Experimental Constraints on the Deep Magma Feeding System at StromboliVolcano, Italy

Michel Pichavant, Ida Di Carlo, Yann Le Gac, Silvio G. Rotolo, Bruno Scaillet

JOURNAL OF PETROLOGY | VOLUME 50 | NUMBER 4 | PAGES 601–624 | 2009 | doi:10.1093/petrology/egp014

Experimental Constraints on the Deep Magma Feeding System at Stromboli Volcano, Italy

MICHEL PICHAVANT[1]*, IDA DI CARLO[2], YANN LE GAC[1], SILVIO G. ROTOLO[2] AND BRUNO SCAILLET[1]

[1]CNRS/INSU, UNIVERSITE D'ORLEANS, UNIVERSITE FRANCOIS RABELAIS TOURS, INSTITUT DES SCIENCES DE LA TERRE D'ORLEANS (ISTO), UMR 6113, 1A RUE DE LA FEROLLERIE, 45071 ORLEANS CEDEX 2, FRANCE
[2]UNIVERSITÀ DI PALERMO, DIPARTIMENTO DI CHIMICA E FISICA DELLA TERRA (CFTA), VIA ARCHIRAFI, 36, 90123 PALERMO, ITALY

RECEIVED MARCH 4, 2008; ACCEPTED FEBRUARY 26, 2009
ADVANCE ACCESS PUBLICATION MARCH 30, 2009

New experiments have been performed on a high-K basalt (PST-9) from Stromboli volcano, Italy, to constrain the physical conditions of golden pumice magmas at their storage level and discuss their petrogenesis. Fluid-present, H_2O- and CO_2-bearing, near-liquidus experiments were performed at 1150°C between 100 and 400 MPa and under oxidizing conditions. Glasses were analyzed by Fourier transform IR spectroscopy and their H_2O and CO_2 concentrations compared with those in glass inclusions. Most glass inclusions cluster near the 200 MPa isobar, suggesting entrapment at a depth of ~8 km. Golden pumice magmas have viscosities of 7–9 Pa s and densities of 2·48–2·57 g/cm^3. Compositions of experimental fluids coexisting with melts along the liquidus have been estimated by mass balance. They range from CO_2-rich ($XH_2O \sim 0{\cdot}2$) at 400 MPa to H_2O-rich ($XH_2O \sim 0{\cdot}8$) at 100 MPa. The free fluid phase present at the reservoir level has an XH_2O of ~0·6, consistent with equilibration with a near-liquidus golden pumice magma below 300 MPa. Clinopyroxene is the liquidus phase in all high-pressure experiments, either fluid-absent (H_2O) or fluid-present (H_2O–CO_2). In contrast, at 0·1 MPa, cpx and ol appear together on the liquidus and olivines are more Fo-rich (up to 89·1) than those crystallizing at high pressures (up to 87·3). The composition of cotectic liquids multiply saturated in cpx and ol has been experimentally determined. Most pumices and a majority of melt inclusions have compositions of cotectic melts. In contrast, PST-9 plots in the cpx field and is representative of less evolved ankaramitic magmas parental to golden pumices. Melt inclusions trapped in Fo >87 olivines form a group of ultra-calcic compositions plotting in the cpx field, interpreted as boundary layer melts locally generated by cpx dissolution in the deep reservoir. Ankaramitic melts in the Stromboli feeding system are proposed to derive from primitive mantle melts by combined crystallization, mixing, wall-rock interaction and assimilation.

KEY WORDS: *Stromboli; experimental petrology; golden pumice; magma storage; physical properties; ultra-calcic melts*

INTRODUCTION

The compositional variations of magmas, their storage depths and conditions, and their residence time at different crustal levels are crucial for establishing monitoring strategies and forecasting volcanic eruptions (e.g. Peccerillo *et al.*, 2006). In general, understanding the internal structure of volcanoes requires the integration of geophysical, petrological and geochemical data. Experimental petrology is increasingly being used to constrain the structure of deep feeding systems and to determine the pre-eruptive storage conditions in subvolcanic reservoirs (e.g. Rutherford *et al.*, 1985; Martel *et al.*, 1998; Scaillet & Evans, 1999; Hammer *et al.*, 2002; Costa *et al.*, 2004; Scaillet *et al.*, 2008). Together with other approaches such as glass inclusion studies, experiments allow us to constrain precisely parameters such as pressure (P), temperature (T) and volatile fugacities (fO_2, fS_2, fH_2O). Because these parameters exert a first-order control on the physical

*Corresponding author. E-mail: pichavan@cnrs-orleans.fr

properties (e.g. density, viscosity) of magmas, their precise knowledge is necessary for eruption models. Although experimental studies on active volcanic systems have so far mainly concerned relatively evolved compositions, basaltic systems are now beginning to be investigated with this approach (Pichavant *et al.*, 2002*a*; Di Carlo *et al.*, 2006).

Stromboli volcano, in the Aeolian arc, Italy, is a reference example of a persistently active basaltic system. The eruptive behaviour of Stromboli is permanently monitored by a combination of geophysical, geochemical and petrological techniques. Simulation tools such as numerical modelling (Longo *et al.*, 2008) and experimental petrology (Di Carlo *et al.*, 2006) have been recently introduced to assist definition of eruptive scenarios and associated risks. Di Carlo *et al.* (2006) have determined the phase relations of a golden pumice sample representative of primitive basaltic magmas of the deep feeding system of Stromboli. A set of pre-eruptive conditions, including pressures between 100 and 270 MPa (average depth of around 7·5 km), temperatures between 1140 and 1160°C, melt H_2O concentrations of ~3 wt % and fO_2 around NNO + 0·5 (where NNO is the nickel–nickel oxide buffer), has been determined for the near-liquidus evolution of golden pumice melts (Di Carlo *et al.*, 2006). Clinopyroxene (cpx) was found to precede olivine (ol) in the crystallization sequence, thus making golden pumice melts resemble ankaramitic liquids from arc settings (Schiano *et al.*, 2000; Médard *et al.*, 2004).

To place more precise constraints on the deep feeding system of Stromboli volcano and to extend the experimental coverage on a magma composition representative of volatile-rich, primitive, arc basaltic liquids worldwide, we report in this paper additional experiments on one golden pumice sample. The new experimental data are combined with previous results and a model for the deep feeding system of Stromboli is presented. Previous phase equilibrium experiments (Di Carlo *et al.*, 2006) were performed with only one volatile component added (H_2O); fluid-absent conditions were imposed. In this paper, additional fluid-absent H_2O-bearing experiments are reported. These place further constraints on the stability of olivine and on the location of ol–cpx cotectics, thus allowing the origin of golden pumice melts to be discussed. However, as a fluid phase is likely to be present at depth in the Stromboli feeding system (Allard *et al.*, 1994; Scaillet & Pichavant, 2005), fluid-present experiments with H_2O–CO_2 mixtures were also performed. Results of these experiments considerably tighten previous estimates on the depth of the reservoir source of golden pumice melts (Di Carlo *et al.*, 2006), and allow the composition of magmatic fluids present at depth in the Stromboli feeding system (Allard *et al.*, 1994; Burton *et al.*, 2007) to be estimated.

VOLCANOLOGICAL AND PETROLOGICAL BACKGROUND

Stromboli is the northernmost volcano of the Aeolian arc, southern Italy (Fig. 1). The Aeolian Archipelago is a volcanic province related to the subduction of the Ionian microplate beneath the Tyrrhenian domain along a front of around 300 km (Chiarabba *et al.*, 2008). Within this regional framework, the volcanological history and magma evolution at Stromboli has been divided into several periods characterized by various extents of K enrichment, from early erupted calc-alkaline (*c.* 160 ka), intermediate high-K calc-alkaline and shoshonites to late K-rich products, the maximum K enrichment being attained during the Neostromboli period (13–6 ka BP, Francalanci *et al.*, 1989, 1993; Hornig-Kjarsgaard *et al.*, 1993). Products erupted during the last 6 kyr, including those emitted during the present-day activity, are shoshonitic to high-K basalts (Francalanci *et al.*, 2004, and references therein).

Stromboli is famous in the volcanological literature for its persistent explosive activity (Rosi *et al.*, 2000), which is associated with continuous degassing. Typical eruptions consist of intermittent low-energy explosions (3–6 events per hour) throwing jets of crystal-rich scoria, gas and ash to heights <150 m above the summit vents. This normal activity can be interrupted by effusive eruptions, such as during 2002–2003 (Ripepe *et al.*, 2005) and 2007, and by major explosions and eruptive paroxysms (Barberi *et al.*, 1993; Speranza *et al.*, 2004; Metrich *et al.*, 2005). These latter occur, respectively, 0·5–3 times per year and 1–10 times per century. During these highly energetic eruptive events, fallouts of meter-sized ballistic blocks are produced together with lapilli showers that extend to distances of several hundreds of meters from the craters. Major explosions and paroxysms are characterized by the eruption of two magma types: a highly vesicular pumice, yellowish in colour (golden pumice), and a black scoria. The pumices are typically crystal-poor (~10 vol. % crystals, e.g. Metrich *et al.*, 2001) whereas the scoria is porphyritic (~50 vol. % crystals, Landi *et al.*, 2004). Despite their differences in crystal content, the golden pumice (hereafter designated as low-porphyricity or LP magmas) and black scoria (hereafter designated as high-porphyricity or HP magmas) bulk-rock compositions are similar to each other (high-K to shoshonitic basalt, Francalanci *et al.*, 2004).

Both golden pumices and black scoriae contain phenocrysts of clinopyroxene, olivine and plagioclase (plag). Clinopyroxene phenocryst compositions divide into two groups, one diopsidic (Mg-number = 0·83–0·91) and the other augitic (Mg-number = 0·70–0·79, Metrich *et al.*, 2001; Francalanci *et al.*, 2004; Di Carlo *et al.*, 2006; M. Pompilio, personal communication). Similarly, olivine phenocryst compositions include two main populations,

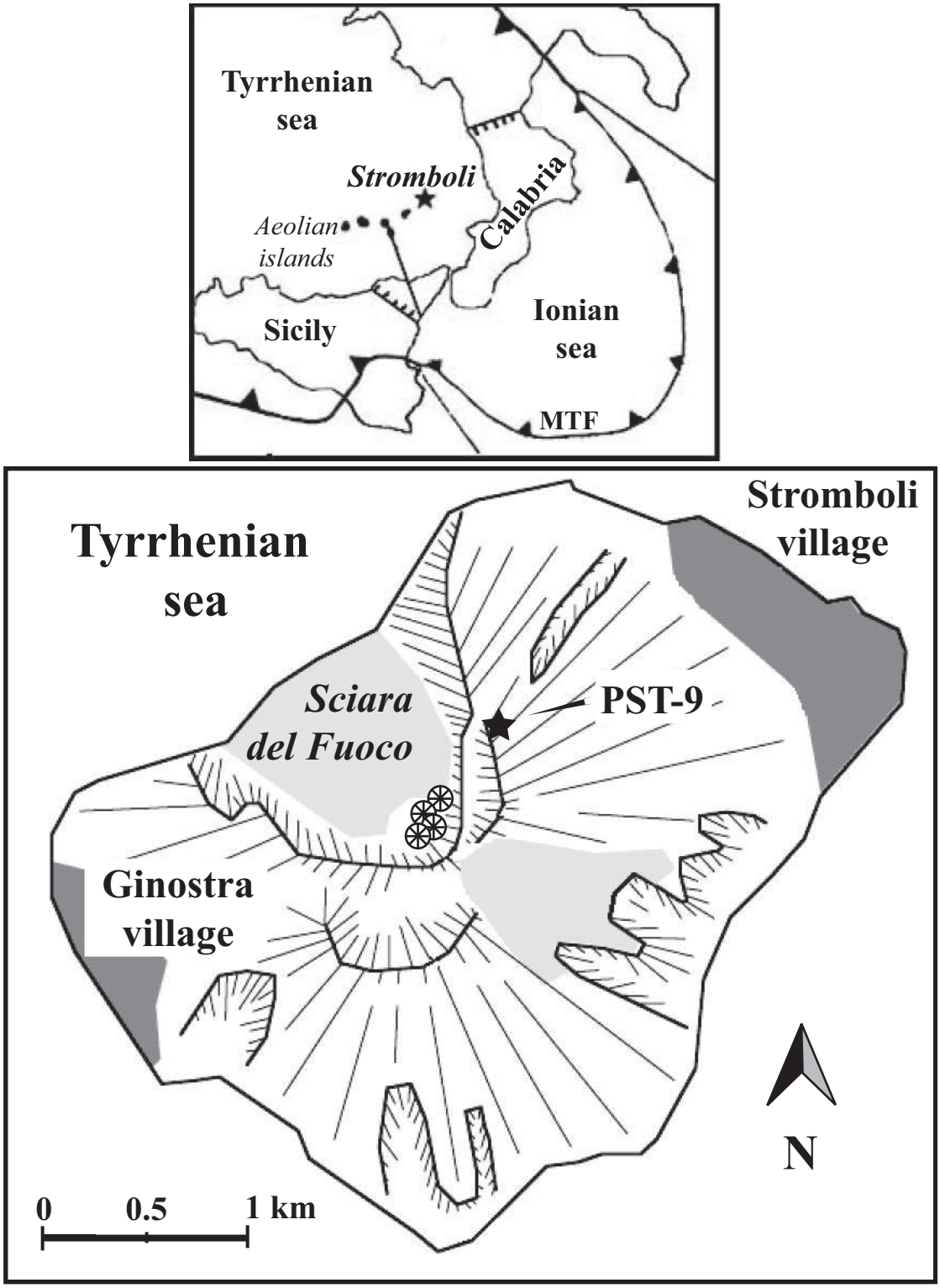

Fig. 1. Top: geographical and geodynamic context of Stromboli, Aeolian Islands, southern Italy. MTF, Main Thrust Front. Bottom: map of Stromboli island showing locations of volcanic units, active craters and villages. The provenance of the PST-9 starting golden pumice sample is also indicated (see also Di Carlo *et al.*, 2006).

$Fo_{78–91}$ and $Fo_{64–74}$ (Metrich *et al.*, 2001; Bertagnini *et al.*, 2003; Francalanci *et al.*, 2004; Di Carlo *et al.*, 2006). For both clinopyroxene and olivine phenocrysts, compositional gaps are apparent around Mg-number = 0·8 and Fo_{75}, respectively (see Metrich *et al.*, 2001, fig. 4; Francalanci *et al.*, 2004, figs 3 and 4; Cigolini *et al.*, 2008, fig. 5). Thus, phenocryst crystallization is discontinuous in the Stromboli feeding system, with cpx and ol crystallizing essentially during two main stages. Diopside and Fo-rich ol phenocrysts are mostly found in golden pumices, and augites and less Fo-rich ol in black scoriae. However, LP and HP magmas can mix extensively during paroxysms, resulting in the incorporation of crystals from one magma into the other (e.g. augitic cpx and Fo-poor ol in golden pumices, e.g. Metrich *et al.*, 2001; Francalanci *et al.*, 2004; Di Carlo *et al.*, 2006). Plagioclase ($An_{60–90}$), the most abundant phenocryst of black scoriae, occurs in golden pumices as reacted crystals (Landi *et al.*, 2004).

Melt inclusions (MI) in golden pumices contain high concentrations of volatiles (H_2O 1·8–3·4%, CO_2 707–1887 ppm, S 610–2500 ppm, Cl 980–2640 ppm, F 641–1364 ppm; Metrich *et al.*, 2001, 2005; Bertagnini *et al.*, 2003). Entrapment pressures from <300 to >400 MPa were calculated (Metrich *et al.*, 2001; Bertagnini *et al.*, 2003) by using the H_2O–CO_2 solubility model of Papale (1999), and from 240 to 300 MPa by using Volatilecalc (Newman & Lowenstern, 2002; Metrich *et al.*, 2005). Black scoriae are instead characterized by volatile-poor MI (e.g. $H_2O \leq$ 0·2%), suggesting trapping of an extensively degassed melt at very low pressures (~10 MPa). Phenocryst composition and MI data strongly suggest that black scoriae represent the shallow-level resident magma feeding the normal Strombolian activity. The resident magma is periodically injected with volatile-rich, crystal-poor magmas emitted as golden pumice during paroxysms and major explosions (e.g. Metrich *et al.*, 2001; Bertagnini *et al.*, 2003; Francalanci *et al.*, 2004).

As regards the degassing activity, the total gaseous output at Stromboli is in the range 6000–12 000 tons/day with $H_2O > CO_2 > SO_2 \gg HF$, HCl (Allard *et al.*, 1994). Stromboli is, together with Etna, one of the major contributors to the Earth's SO_2 volcanogenic budget, the CO_2/SO_2 ratio in the plume being around eight during quiescent degassing and increasing to 16–30 during explosions (Burton *et al.*, 2007). Scaillet & Pichavant (2005) and Burton *et al.* (2007) have suggested that a free fluid phase is present at depth in the Stromboli plumbing system.

EXPERIMENTAL STRATEGY

To better constrain the depth and conditions in the deep-seated reservoir beneath Stromboli, new (1) high-pressure, fluid-present experiments, (2) high-pressure, olivine-added experiments and (3) 0·1 MPa experiments have been performed. In all these experiments, the starting material is the golden pumice sample PST-9 (Table 1) previously used by Di Carlo *et al.* (2006).

Table 1: Composition of PST-9 golden pumice and starting glass

Label	PST-9[1]	Glass[2] ($n = 98$)[3]
SiO_2	49·4	50·2(3)[4]
TiO_2	0·79	0·84(4)
Al_2O_3	15·75	15·2(3)
Fe_2O_3	1·3	n.d.
FeO	6·5	7·81(33)
MnO	0·15	0·16(5)
MgO	7·96	7·87(12)
CaO	12·73	12·4(2)
Na_2O	2·27	2·29(5)
K_2O	1·85	1·86(6)
P_2O_5	0·43	0·64(6)
Cr_2O_3	–	0·05(5)
NiO	–	0·03(3)
Total	99·1	99·4

[1]Whole-rock analysis. Major elements (wt %) analysed by inductively coupled plasma atomic emission spectrometry (ICP-AES); total includes LOI (loss on ignition) = 0·62 wt %; trace elements analysed by inductively coupled plasma mass spectrometry (ICP-MS; Cr 259 ppm; Ni 75 ppm; Ba 920 ppm; La 45 ppm; Eu 2·0 ppm; Lu 0·3 ppm). Analysis performed at the Centre de Recherches Pétrographiques et Géochimiques (CRPG, Nancy, France).
[2]Electron microprobe analysis of PST-9 glass.
[3]Number of electron microprobe analyses.
[4]One standard deviation in terms of last digit.

Experiments of the first type (i.e. fluid-present H_2O–CO_2 experiments) were designed to locate the liquidus of the golden pumice in presence of H_2O–CO_2 fluids, to complement the fluid-absent hydrous crystallization experiments of Di Carlo *et al.* (2006). They were performed at a constant temperature (1150°C), for three pressures (400, 200 and 100 MPa; thought to bracket the pressure of the deep reservoir), and for various $H_2O/(H_2O + CO_2)$ ratios. The temperature chosen corresponds to the average pre-eruptive storage temperature of golden pumice melts, as defined from the combination of homogenization temperatures (Metrich *et al.*, 2001) and liquidus curves (Di Carlo *et al.*, 2006). Comparison between the H_2O and CO_2 concentrations of experimental glasses and of glass inclusions in golden pumices (Metrich *et al.*, 2001, 2005; Bertagnini *et al.*, 2003) allows pressures of trapping of glass inclusions to be directly evaluated. Finally, the determination of the composition (H_2O/CO_2) of experimental fluids coexisting with golden pumice melts places strong constraints on the fluid composition at depth in the

Stromboli feeding system, which can be compared with that inferred from the monitoring of volcanic gases (Allard *et al.*, 1994; Burton *et al.*, 2007).

The two other types of experiments were performed to define more precisely the conditions of olivine stability in golden pumices and the composition of ol–cpx cotectic melts. High-pressure, fluid-absent, olivine-added experiments were conducted at 400 MPa to check the crystallization sequence determined by Di Carlo *et al.* (2006), and to constrain the composition of ol–cpx cotectic melts at 1150°C. Near-liquidus experiments were performed at 1 atm to complement the high-pressure data. They extend the experimental information about olivine stability and composition of ol–cpx cotectic melts to pressures <50 MPa and melt H_2O concentrations <1 wt % (Di Carlo *et al.*, 2006).

STARTING ROCK SAMPLE

PST-9 is a strongly vesicular (vesicles *c.* 60 vol. %) K-basalt, with 49·4 wt % SiO_2 and 1·85 wt % K_2O (Table 1). TiO_2 content (0·79 wt %) is low, whereas CaO and CaO/Al_2O_3 contents are both high (respectively 12·7 wt % and 0·81, Table 1). Concentrations of compatible oxides and trace elements are relatively elevated (7·96 wt % MgO, 259 ppm Cr, 75 ppm Ni, Table 1). PST-9 is chemically extreme in the group of Stromboli golden pumices; it has the highest MgO, CaO and CaO/Al_2O_3, the lowest FeO_t and, consequently, the highest Mg-number of all golden pumices. The groundmass composition (49·6 wt % SiO_2, 2·07 wt % K_2O, 6·41 wt % MgO and $CaO/Al_2O_3 = 0·66$, Di Carlo *et al.*, 2006) is also distinctive, being the highest in MgO, CaO/Al_2O_3 and Mg-number, and the lowest in FeO_t of all golden pumice groundmasses (Metrich *et al.*, 2001, 2005; Bertagnini *et al.*, 2004; Francalanci *et al.*, 2004; Di Carlo *et al.*, 2006).

PST-9 is slightly porphyritic (*c.* 11 vol. % crystals), in a range typical for pumices (10–12 vol. %, Metrich *et al.*, 2001, p. 1474). Modal proportions, determined by point-counting (vol.%, vesicle-free basis), are 89% glass, 8% clinopyroxene, 1–2% olivine and 1–2% plagioclase. Crystals present include cognate phenocrysts (cpx, ol) and xenocrysts (cpx, ol, plag) inherited from the crystal-rich scoriae (Di Carlo *et al.*, 2006). The low plagioclase abundance implies limited syneruptive incorporation of HP crystals because plagioclase is the dominant phenocryst phase in HP magmas. Additional constraints on the proportion of phenocrysts and xenocrysts in PST-9 come from mass-balance calculations, performed using whole-rock, groundmass glass and crystal compositions. For cpx and ol, electron microprobe compositions of either phenocrysts or xenocrysts (Di Carlo *et al.*, 2006, table 1) were considered. Plag compositions in the range measured for xenocrysts (Landi *et al.*, 2004) were tested. The most satisfactory calculations (i.e. those yielding the minimum differences between computed phase proportions and point-counting data) were obtained for diopsidic cpx and Fo_{88} ol (i.e. for cpx and ol phenocryst compositions) and for plag in the range $An_{80–88}$. For An_{88}, the computed proportions (wt %) are 9·5% cpx, 1·5% ol and <0·5% plag, and the computed bulk K_2O concentration is within 1% relative of the whole-rock value. In contrast, calculations with the same plag but with cpx and ol xenocryst compositions yield 14% cpx, 2% ol and 5 wt % plag, in clear disagreement with the point-counting data. The computed K_2O concentration is also too low by >10% relative. Therefore, the crystal population in PST-9 is dominantly composed of diopsidic cpx and Fo-rich ol phenocrysts. The fact that the PST-9 groundmass is chemically distinctive from groundmasses of other golden pumices rules out the possibility that the extreme whole-rock chemistry of PST-9 is controlled uniquely by a high abundance of xenocrysts inherited from HP magmas.

PST-9 was selected as starting material because it is the most primitive golden pumice (Metrich *et al.*, 2001, 2005; Bertagnini *et al.*, 2004; Francalanci *et al.*, 2004; Di Carlo *et al.*, 2006). Whole-rock pumices have CaO/Al_2O_3 between 0·52 and 0·81 whereas that of melt inclusions ranges from around 0·64 to >1. For comparison, the CaO/Al_2O_3 of the PST-9 whole-rock and groundmass are 0·81 and 0·66, respectively. As this study is aimed at discussing the genesis of golden pumice as well as the significance of melt inclusions, the use of primitive starting compositions is mandatory. PST-9 and STR9/96d (Francalanci *et al.*, 2004) are the two only golden pumices in the database with MgO >7 wt % and CaO/Al_2O_3 in the middle of the melt inclusion range. However, mass-balance calculations similar to those performed above (data of Francalanci *et al.*, 2004) show that STR9/96d has an unusually high proportion of ol crystals. PST-9 is also compositionally extreme but, as emphasized below, the main aspects of the early crystallization of golden pumices such as order of phase appearance and cpx:ol proportions are reproduced by using PST-9 as starting material.

EXPERIMENTAL METHODS

PST-9 pumice was first ground in an agate mortar to ~50 μm, then fused in air at 1400°C, 0·1 MPa in a Pt crucible. Two cycles of melting of 2–4 h each (with grinding between) were performed, yielding a homogeneous glass whose composition was checked by electron microprobe (Table 1). The glass was then crushed to ~10–50 μm and stored in an oven.

High-pressure experiments

$Au_{70}Pd_{30}$ capsules (15 mm length, 2·5 mm internal diameter, 0·2 mm wall thickness) were used as containers. For the fluid-present experiments, charges consisted of glass powder (about 30 mg), distilled water and $Ag_2C_2O_4$

Table 2: High-pressure experimental results

Charge no.	XH_2O_{in}.	H_2O melt (wt %)	aH_2O[1]	log fO_2	ΔNNO	Fluid[2] (wt %)	XH_2O	Silicate phases[3]	ΣR^2	ΔFeO[4]	$K_d^{Fe-Mg}{}_{cpx-l}$	$K_d^{Fe-Mg}{}_{ol-l}$
Run 17, 1150°C, 408 MPa, 17 h, fH_2 = 0·94 MPa, X_{Ni} = 0·35												
17-1	0·80	5·09[5]	0·69	−7·3	+0·9	4	0·42	gl(100)	2·84	−17·6		
17-2	0·45	4·82[5]	0·65	−7·4	+0·8	20	0·22	gl(100)	3·28	−20·1		
17-3	0·63	4·11[5]	0·54	−7·5	+0·7	6	0·10	gl(99) + cpx(1)	2·48	−20·2	0·30/0·23	
17-4[6]	—	3·37[5]	0·40	−7·8	+0·4	0	—	gl + ol + cpx + qu	n.d.	n.d.	0·34/0·29	0·31/0·23
17-5[6]	—	5·35[5]	0·77	−7·2	+1·0	0	—	gl + ol	n.d.	n.d.		0·36/0·25
Run 22, 1150°C, 201 MPa, 5 h, fH_2 = 0·016 MPa, X_{Ni} = 0·04												
22-1	0·89	3·06[5]	0·58	−4·7	+3·6	7	0·83	gl(100)[7]	0·05	−1·3		
22-2	0·81	2·33[5]	0·39	−5·0	+3·3	8	0·75	gl(98) + cpx(2)[7]	0·04	−0·4	0·68/0·42	
22-3	0·68	2·36[5]	0·39	−5·0	+3·3	7	0·54	gl(96) + cpx(4)[7]	0·11	−3·9	0·52/0·40	
Run 23, 1150°C, 88·4 MPa, 12 h, fH_2 = 0·007 MPa, X_{Ni} = 0·04												
23-1	0·91	2·52[5]	0·74	−4·5	+3·8	9	0·88	gl(100)[8]	0·18	−2·5		
23-2	0·82	2·38[5]	0·68	−4·6	+3·7	8	0·75	gl(99) + cpx(1)[8]	0·52	−6·7	0·52/0·60	
23-3	0·76	2·23[5]	0·61	−4·7	+3·6	8	0·67	gl(99) + cpx(1)[8]	0·15	−3·6	0·63/0·62	
23-4	0·53	1·63[5]	0·35	−5·1	+3·2	n.d.	n.d.	gl(90) + cpx(10)[8]	0·07	−2·3	0·55/0·60	

All experiments performed with PST-9 glass starting material. XH_2O_{in}. is initial molar $H_2O/(H_2O + CO_2)$ in the charge. XH_2O is equilibrium molar $H_2O/(H_2O + CO_2)$ in the fluid, calculated by mass balance (see text). $K_d^{Fe-Mg}{}_{cpx-l}$ = (Fe/Mg in cpx)/(Fe/Mg in melt); $K_d^{Fe-Mg}{}_{ol-l}$ = (Fe/Mg in ol)/(Fe/Mg in melt). The first K_d is calculated with FeO = FeO and the second with FeO = FeO_t (see text). n.d., not determined.
[1]aH_2O calculated from H_2O melt using the model of Burnham (1979) and melt compositions from Table 4; X_{Ni} is mole fraction of Ni in the alloy phase of the sensor; log fO_2 calculated from experimental fH_2 and fH_2O (determined from aH_2O); ΔNNO = log fO_2 − log fO_2 of the NNO buffer calculated at experimental P and T (Pownceby & O'Neill, 1994).
[2]Proportion of fluid present in the charge calculated (see text) as per cent mass of fluid/(mass of fluid + mass of melt).
[3]Proportions (wt %) of silicate phases present calculated by mass balance; gl, glass; cpx, clinopyroxene; ol, olivine; qu, quench crystals detected by SEM.
[4]Apparent loss or gain of FeO (Fe = FeO_t) calculated as $100 \times (FeO_{calc} - FeO_{starting\ sample})/FeO_{starting\ sample}$. FeO_{calc} and ΣR^2 are obtained from the mass-balance calculations.
[5]H_2O concentration from Table 5.
[6]San Carlos olivine added to the starting mixture.
[7]Approximately 1–3 wt % Fe–Ti oxide phase present.
[8]Approximately 3–5 wt % Fe–Ti oxide phase present.

as the source of CO_2. Water was introduced with a microsyringe before adding $Ag_2C_2O_4$ and the glass powder. Water and $Ag_2C_2O_4$ were weighed so as to generate charges with variable XH_2O_{in}. [initial molar $H_2O/(H_2O + CO_2)$ = 0·53–0·91, Table 2]. The $(H_2O + CO_2)/(H_2O + CO_2 + glass)$ mass ratio was kept constant constant at ~0·1 (see Holtz *et al.*, 1992), except for charge 17-2 (~0·25). For the fluid-absent, olivine-added experiments, charges consisted of pre-mixed glass powder plus multiple sieved San Carlos olivine grains (Fo ~91, size around 50 μm), and distilled water. All capsules were sealed by arc welding, keeping them in a liquid nitrogen bath to prevent water loss. They were then put in an oven for several hours and reweighed to check for leaks. Three to four capsules with differing XH_2O_{in}. were run together in the same experiment. The 400 MPa fluid-present experiment also included the two fluid-absent olivine-added capsules 17-4 and 17-5 (Table 2). For each experiment, a separate Ni–Pd–O sensor capsule was included for the determination of the experimental fH_2. It consisted of two pellets of NiPd metal mixtures (each with different Ni/Pd ratio) plus NiO, placed in either a Pt or a AuPd capsule in presence of excess H_2O (Taylor *et al.*, 1992).

The three high-pressure experiments were carried out in the same internally heated pressure vessel as used by Di Carlo *et al.* (2006), working vertically and pressurized with Ar–H_2 mixtures obtained by sequential loading of H_2 and Ar at room temperature (Scaillet *et al.*, 1992). Experiment 17 (Table 2) was performed with an initially applied pressure of 1 bar H_2 whereas, for the two others (experiments 22 and 23), no H_2 was initially added. Total pressure was recorded by a transducer calibrated against a Heise gauge (uncertainty ± 20 bars). A double winding molybdenum furnace was used, allowing near-isothermal conditions in the 2–3 cm long hotspot (gradient <2–3°C/cm). Temperature was measured using three

type S thermocouples and recorded continuously (uncertainty ± 5°C). The experiments lasted for 17, 5 and 12 h (Table 2). They were drop-quenched at essentially constant pressure (Di Carlo *et al.*, 2006), resulting in quench rates of ~100°C/s.

At the end of the experiment, capsules were weighed to check for leaks and then opened. For each PST-9 capsule, fragments of the run products were mounted in epoxy and polished for scanning electron microscope (SEM) observations and electron microprobe analyses. Double polished thin sections were prepared for Fourier transform IR spectroscopy (FTIR) analyses. For the sensor capsule, the metallic pellets were recovered, mounted in epoxy and then analyzed by electron microprobe.

The fO_2 of the sensor capsule was determined from the final composition of the metallic phase (Pownceby & O'Neill, 1994). Then, the fH_2 of the sensor capsule (and by inference of the experiment, as fH_2 is identical for all capsules) was calculated from the water dissociation equilibrium, using the fO_2 determined above, the dissociation constant of water (Robie *et al.*, 1979), and the fugacity of pure water at the experimental P and T (Ferry & Baumgartner, 1987; Holloway, 1987). Table 2 lists sensor compositions (mole fraction of Ni in the metallic phase, X_{Ni}) and the corresponding fH_2 for each experiment.

For a given experiment (i.e. constant P–T–fH_2), the fO_2 of each individual charge varies with aH_2O (or fH_2O). The latter was determined for each charge from the H_2O content of the quenched glass, measured by FTIR. H_2O concentrations in glass were converted to fH_2O by using the thermodynamic model for H_2O solution in multicomponent melts of Burnham (1979). The oxygen fugacity of each charge was calculated from the water dissociation equilibrium, using the fH_2 and fH_2O determined above, and the dissociation constant of water (Robie *et al.*, 1979). Typical uncertainty on log fO_2 is less than 0·25 log units (e.g. Scaillet *et al.*, 1995; Martel *et al.*, 1999; Scaillet & Evans, 1999; Costa *et al.*, 2004; Di Carlo *et al.*, 2006). In this study, fO_2 values are expressed as deviations from the NNO buffer (ΔNNO values), calculated at the P and T of interest.

0·1 MPa experiments

They were carried out in a vertical furnace using the wire-loop method. Pt suspension wires (0·2 mm in diameter) were used. The fO_2 was controlled by CO–CO_2 gas mixtures monitored by certified electronic flowmeters. A ZrO_2 electrochemical cell provided direct fO_2 readings; the uncertainty on fO_2 is better than 0·1 log unit. Most experiments were performed at NNO + 0·5; one was conducted at NNO − 1·5 to test the influence of fO_2 on the composition of near-liquidus clinopyroxene. Temperature was monitored using an S-type thermocouple placed adjacent to the sample, and is controlled to better than 2°C. Experiments were drop-quenched electrically.

Each experiment was repeated several times at the same temperature and fO_2, and with the same Pt suspension wire, using PST-9 glass as starting material. It was found that three equilibration cycles of 3 h each allowed steady-state Fe concentrations to be attained in both glasses and Pt suspension wires. Equilibration cycles of longer durations led to K_2O loss from the charge and were avoided. Charges resulting from the two first equilibration cycles were dissolved in a warm HF bath before placing the fresh starting glass powder on the wire. The charge from the third equilibration cycle was mounted in epoxy together with the suspension wire and polished for SEM observations and electron microprobe analyses.

ANALYTICAL METHODS

Major elements

All charges were systematically examined by SEM in backscattered electron mode to assist in the identification of the mineral phases, determine the textural relationships between them and evaluate the importance of quench crystallization, if any. Instruments from the universities of Palermo (Cambridge LEO 440) and Orléans (JEOL WINSET JSM 6400) were both used. Electron microprobe analyses were performed with either the Cameca Camebax or the Cameca SX-50 of the joint BRGM–CNRS facility at Orléans. Analyses were carried out under an acceleration voltage of 15 kV, a counting time of 10 s and a sample current of 6 nA, except for metallic sensor phases and capsules, which were analyzed under 20 kV and 20 nA. For glasses, the beam was defocused to ~10 μm whereas, for minerals, a focused beam (1–2 μm) was used. Silicate minerals were used as standards. Estimated relative analytical errors are 1% for SiO_2, Al_2O_3 and CaO, 3% for FeO, MgO and TiO_2, and 5% for MnO, Na_2O, K_2O and P_2O_5. For each charge, the electron microprobe compositions of the starting glass and of silicate phases present were mass-balanced using a least-squares technique (Albarède, 1995) based on eight major oxides, excluding MnO, P_2O_5 and H_2O. Silicate phase proportions were calculated together with the bulk composition of each charge. Fe loss was obtained from the difference between the starting and the calculated bulk FeO concentration.

H_2O and CO_2

Concentrations of H_2O and CO_2 (as CO_3^{2-}) in glasses were determined by IR spectrometry. A Nicolet Magna 760 spectrometer attached to a NicPlan microscope was used. Spectra were acquired between 650 and 7400 cm^{-1} on doubly polished samples mostly <50 μm thick. An IR light source, a KBr beamsplitter and a liquid nitrogen cooled MCT/A detector were used. Resolution was set to 2 cm^{-1} and spectra were accumulated for 128 scans. Two to five spots (diameter mostly ~100 μm, ~60 μm in a few cases) were analyzed on each sample. Concentrations of

Table 3: 0·1 MPa experimental results

Charge no.	T (°C)	log fO_2[1] (bar)	ΔNNO	Phase assemblage[2]	ΣR^2	△FeO[3] (%)	$K_d^{Fe-Mg}{}_{cpx-l}$	$K_d^{Fe-Mg}{}_{ol-l}$	$K_d^{Ca-Na}{}_{plg-l}$
1	1220	−7·02	0·5	gl(100)	0·62	−7·4	—	—	—
3	1195	−7·29	0·5	gl(100)	1·25	−9·4	—	—	—
4	1190	−7·35	0·5	gl(99) + ol(tr) + cpx(1)	0·22	−5·0	0·18/0·16	0·31/0·23	—
5	1180	−7·46	0·5	gl(99) + ol(−1) + cpx(4) + plg(−2)	0·56	−8·1	0·57/0·51	0·32/0·24	1·20
6	1170	−7·58	0·5	gl(74) + ol(2) + cpx(17) + plg(7)	1·97	−15·9	0·46/0·47	0·29/0·21	1·19
8	1180	−9·46	−1·5	gl(98) + ol(2) + cpx(2) + plg(−2)	2·50	−15·4	0·27/0·24	0·31/0·27	1·10

[1]logfO_2 calculated from the composition of the CO–CO_2 gas mixture; ΔNNO = logfO_2 − logfO_2 of the NNO buffer calculated at the experimental T (Pownceby & O'Neill, 1994).
[2]Phase proportions calculated by mass balance; gl, glass; cpx, clinopyroxene; ol, olivine; plg, plagioclase, tr; trace (phase proportion <0·5% by weight).
[3]Apparent loss or gain of FeO (Fe = FeO_t) calculated as $100 \times (FeO - FeO_{starting\ sample})/FeO_{starting\ sample}$. FeO and R^2 are obtained from the mass-balance calculations.
$K_d^{Fe-Mg}{}_{cpx-l}$ = (Fe/Mg in cpx)/(Fe/Mg in melt); $K_d^{Fe-Mg}{}_{ol-l}$ = (Fe/Mg in ol)/(Fe/Mg in melt); $K_d^{Ca-Na}{}_{plg-l}$ = (Ca/Na in plg)/(Ca/Na in melt). For cpx–melt and ol–melt, the first K_d is calculated with FeO = FeO and the second with FeO = FeO_t (see text).

H_2O and CO_2 were determined from the Beer–Lambert law. Sample thicknesses (determined both microscopically and from interference patterns present in some spectra) are known to 1–2 μm. Densities of experimental glasses were calculated from the density of the anhydrous starting PST-9 glass measured at room conditions ($\rho = 2{\cdot}740 \pm 0{\cdot}006$), together with a partial molar volume of 12 cm^3/mol (Richet *et al.*, 2000) to account for the presence of dissolved H_2O, the effect of dissolved CO_2 on glass density being neglected. For H_2O, the absorbance of the 3510–3530 cm^{-1} band was determined by taking a linear baseline between 3800 and 2500 cm^{-1}. An extinction coefficient (ε^{3530}) of 64 L/mol cm (Metrich *et al.*, 2001) was used. For CO_2, the absorbance of the 1515 cm^{-1} band was measured on background-subtracted spectra (Dixon *et al.*, 1995), the spectrum of an ~40 μm thick PST-9 starting glass being used as background. The method was checked by taking glass from charge 22-2 as background, instead of the starting glass. Results were found to be identical. An extinction coefficient (ε^{1515}) of 363 L/mol cm, calculated from the equation of Dixon & Pan (1995), was used.

EXPERIMENTAL RESULTS

Fe loss and attainment of equilibrium

A total of 12 high-pressure and six 0·1 MPa experimental charges are reported (Tables 2 and 3). Fe loss decreases with increasing fO_2, from around −20% in the five charges from run 17 (ΔNNO = +0·4–1·0), to ≤−5% in the seven charges from runs 22 and 23 (ΔNNO = +3·2–3·8, Table 2). It should be noted that Fe losses reported for runs 22 and 23 are maximum values as the corresponding charges contain an Fe–Ti oxide phase, which was not considered in the mass-balance calculations (see below). At 0·1 MPa, the average Fe loss is −10% (Table 3). Therefore, Fe loss has been effectively minimized but not eliminated in this study.

The high-pressure experiments reported in this paper involve partitioning of volatile components between fluid and melt, crystallization (i.e. mineral synthesis) and mineral dissolution, the last in the olivine-added charges. Fluid–melt experiments have all been performed at the same temperature (1150°C), and the final fluid phase composition was in all cases approached from the H_2O-rich side (i.e. for each fluid-present charge, $XH_2O_{in.} > XH_2O$, Table 2). Reversals of the fluid XH_2O (and also of melt H_2O/CO_2) have not been performed, for example, by two-stage high → low pressure polybaric experiments (see Dixon *et al.*, 1995). Consequently, equilibrium cannot be ascertained in these experiments. However, fluid XH_2O values cover a wide compositional range (from 0·10 to 0·88, Table 2). Both the final fluid XH_2O and the difference between initial and final XH_2O values vary regularly with experimental pressure. The proportion of volatiles in the charge [i.e. the $(H_2O + CO_2)/(H_2O + CO_2 + glass)$ mass ratio in run 17-2 is more than twice that in the other fluid-present charges] has no influence on the final composition of the fluid and melt phases. The FTIR data show that both H_2O and CO_2 are distributed homogeneously in the glasses (see below and Table 5). Our experimental durations are also much longer (5–17 h, Table 2) than the 2 h sufficient for attainment of equilibrium in comparable fluid–melt experiments using glass powder starting materials (Dixon *et al.*, 1995). Therefore, equilibrium partitioning of H_2O and CO_2 between melt and fluid phases was most probably attained.

Crystal–liquid equilibrium was approached from above the liquidus in the crystallization experiments and from below the liquidus in the olivine dissolution experiments. Both crystallization (of cpx) and dissolution (of ol) occurred simultaneously in one charge (17-4, Table 2). When present, crystals (mainly clinopyroxene) are euhedral and homogeneously distributed within the charges. The occurrence of quench crystals in one charge, most probably phlogopite (see below), is an indication of fast nucleation and growth in the crystallization experiments. For hydrous basaltic systems, experimental durations as in this study are sufficient for equilibrium phase assemblages and proportions of crystals to be obtained (see discussion by Di Carlo *et al.*, 2006). In this study, both experimental clinopyroxene and olivine are chemically homogeneous and their crystal–liquid exchange coefficients (K_d) are in general agreement with literature values (see below). Finally, all charges from the crystallization experiments were successfully mass balanced: positive phase proportions were obtained; the low ΣR^2 values (0·04–0·52, Table 2) indicate small differences between starting and calculated silicate compositions. Overall, these different lines of evidence suggest a close approach toward equilibrium in the crystallization experiments.

In the ol dissolution experiments, the composition of glass <10 μm of the ol–glass interface is identical to the composition of the far-field glass. This demonstrates that there is no mass transfer in the melt adjacent to dissolving ol crystals at the end of the experiments. Because, in non-convecting systems, ol dissolution proceeds by chemical diffusion in the melt (interface kinetics are extremely fast; e.g. Zhang *et al.*, 1989), the lack of any mass transfer implies that ol dissolution has ceased. Therefore, time was sufficient for ol dissolution to reach at least a steady state. Assuming that ol dissolution is rate-limited by diffusion of Si in the melt and taking D_{Si} from Watson (1994), diffusion distances around 500 μm are calculated. These values are consistent with the lack of chemical zonation in glass from the ol dissolution experiments, given that these charges started from glass powder pre-mixed with multiple ol grains. One important point is that phase assemblages and melt compositions in the dissolution experiments are consistent with those in the crystallization experiments performed at the same P and T (experiment 17, 408 MPa, 1150°C, Table 2). In fact, the 1150°C ol + cpx cotectic (Figs. 3 and 4) has been located by combining constraints from both types of charges. This agreement constitutes a positive test of reversibility for the attainment of crystal–liquid equilibrium in our experiments. Therefore, a close approach toward crystal–liquid equilibrium from both sides can be demonstrated at least for experiment 17.

In comparison with the high-pressure experiments, the 0·1 MPa crystallization charges showed some deviations from equilibrium. For several charges, negative phase proportions were obtained by mass balance (Table 3), suggesting either disequilibrium phase assemblages or, more probably, equilibrium phase assemblages but incomplete chemical equilibration. The $K_d^{Fe-Mg}{}_{ol-l}$ values in the 0·1 MPa charges are in agreement with both the high-pressure (Table 2) and the literature data (see below), as is also the case for the $K_d^{Fe-Mg}{}_{cpx-l}$ values in the NNO − 1·5 charge (Table 3). However, the three 0·1 MPa NNO + 0·5 charges have variable $K_d^{Fe-Mg}{}_{cpx-l}$ (Table 3; see also below), which contrasts with their homogeneous $K_d^{Fe-Mg}{}_{ol-l}$ and indicates that cpx grains are heterogeneous and/or zoned in these charges. Despite these equilibration problems, the 0·1 MPa experimental results are internally consistent, and although not directly applicable to the Stromboli magmas, which are volatile-bearing, provide useful experimental data at this reference pressure.

Liquidus phase equilibria and compositions

Stable crystalline phases in the high-pressure experiments include clinopyroxene (relatively small in size, 10–20 μm), olivine (residual from the starting mixture in the two olivine-seeded charges), and an oxide phase present in all charges from runs 22 and 23 (Table 2). This phase, most probably an Fe–Ti oxide (Di Carlo *et al.*, 2006), could not be reliably analyzed by electron microprobe because of its very small size. Consequently, its proportion is not constrained by mass balance. We estimate that it amounts to around 1–2 wt % in charges from run 22, and up to 3–5 wt % in charges from run 23. Quench phases were detected by SEM in only one charge (17-4, Table 2). These appear as very thin needles (most probably phlogopite) nucleating on clinopyroxene crystals (see Di Carlo *et al.*, 2006). However, these quench phases are present in minor amounts. We thus conclude that quench crystallization has a negligible influence in this study. In the 0·1 MPa experiments, stable phases present include ol, cpx and plag.

The liquidus silicate phase in the high-pressure fluid-present experiments is clinopyroxene. At 1150°C and for the three pressures investigated, clinopyroxene is the first silicate phase to appear when XH_2O_{in}. is progressively reduced (Table 2). Olivine was not observed in the fluid-present charges, which are generally crystal-poor. A maximum of 10 wt % cpx is present in charge 23-4 (Table 2). For comparison, under fluid-absent conditions at 400 MPa and 1150°C, a minimum of 12 wt % cpx crystallized before ol joined cpx on the liquidus (Di Carlo *et al.*, 2006). Therefore, at 400 MPa, the crystallization sequence is identical (cpx then ol) in the fluid-present (this study) and fluid-absent (Di Carlo *et al.*, 2006) experiments. The addition of CO_2 has no detectable influence on the crystallization sequence of PST-9 golden pumice at this pressure.

At 400 MPa and 1150°C, the fluid-present liquidus (equivalent to cpx saturation) is bracketed by charges 17-3 and 17-2 (Table 2). The corresponding melt H_2O concentration range is slightly narrower than that for the

fluid-absent, olivine-added liquidus (4·11–4·82 vs 3·37–5·35 wt % H_2O, Table 2). The fluid-absent ol-free liquidus was previously located between 3·5 and 4 wt % H_2O in the melt using the by-difference method (Di Carlo *et al.*, 2006). Therefore, at 400 MPa and 1150°C, neither the presence of CO_2 nor changes of the melt composition induced by forced olivine saturation significantly influence the H_2O concentration of liquidus melts. At 200 and 100 MPa, the H_2O concentrations of the fluid-present 1150°C liquidus melts (~2·7 and 2·4 wt %, respectively, Table 2) are in excellent agreement with the H_2O concentrations of the fluid-absent 1150°C liquidus melts (Di Carlo *et al.*, 2006). Therefore, our experimental data demonstrate that, at 1150°C and between 100 and 400 MPa, the fluid-present and fluid-absent liquidi essentially coincide when compared at the same melt H_2O content and pressure. This implies that the presence of CO_2 does not significantly shift the position of the PST-9 liquidus in the P–T–H_2O melt space.

In all experiments, clinopyroxene is Mg-rich, Cr-bearing, and Ti- and Al-poor. Cpx from charge 17-3 (400 MPa) and charge 4 (0·1 MPa) have the highest Cr and lowest Ti of the PST-9 cpx experimental database, being compositionally similar to diopsidic clinopyroxenes from golden pumices (Francalanci *et al.*, 2004; Di Carlo *et al.*, 2006; M. Pompilio, unpublished data). These cpx, and the one from charge 17-4, plot on the negative trend between Mg-number (calculated with FeO) and ΔNNO (Di Carlo *et al.*, 2006). This confirms the fO_2 estimate for golden pumices (NNO + 0·5, Di Carlo *et al.*, 2006, fig. 8; see also Metrich *et al.*, 2002). For charges with fO_2 below NNO + 2, including the high-pressure and the 0·1 MPa charges, the average cpx–liquid exchange coefficient ($K_d^{Fe-Mg}{}_{cpx-l}$) is 0·35 ± 0·14 ($n = 6$) when calculated with FeO in both cpx (determined from the structural formulae, Lindsley, 1983) and glass [calculated from Kress & Carmichael (1991) using data from Tables 2–4]. This average K_d compares well with literature values for similar fO_2 (0·26–0·31, Sisson & Grove, 1993; 0·32 ± 0·06, Berndt *et al.*, 2005; 0·35 ± 0·07, Di Carlo *et al.*, 2006; 0·29 ± 0·08, Pichavant & Macdonald, 2007). If the three 0·1 MPa NNO + 0·5 charges are excluded (as cpx is slightly heterogeneous in these charges; see above), the average $K_d^{Fe-Mg}{}_{cpx-l}$ agrees even better with previous results (0·31), the standard deviation being drastically reduced (± 0·02). For strongly oxidizing fO_2 (ΔNNO > +3), the fluid-present high-pressure experiments yield a $K_d^{Fe-Mg}{}_{cpx-l}$ of 0·58 ± 0·07 ($n = 5$), distinctly higher than for less oxidizing fO_2 (see also Pichavant *et al.*, 2002a, 2002*b*).

In contrast to the high-pressure results, ol and cpx appear simultaneously on the 0·1 MPa liquidus at 1190°C and NNO + 0·5 (Table 3). No cpx was detected in the 1195°C, NNO + 0·5 charge. Plagioclase (An_{69-76}) is the third phase in the crystallization sequence, being present below 1180°C. Therefore, the crystallization interval is much smaller at 0·1 MPa than at high pressures in the presence of water (Di Carlo *et al.*, 2006). Lowering fO_2 from NNO + 0·5 to NNO − 1·5 at 1180°C does not change the phase assemblage. Olivine in the 0·1 MPa experiments has Fo decreasing with temperature from 89·1 to 87·3, and is more magnesian than olivine in the high-pressure fluid-absent experiments (maximum $Fo_{87·3}$, Di Carlo *et al.*, 2006). Olivine in the high-pressure olivine-added experiments has Fo between 90 and 91 (i.e. is more magnesian than olivine grown at 0·1 MPa from unseeded PST-9). The average olivine–liquid exchange coefficient ($K_d^{Fe-Mg}{}_{ol-l}$) is 0·32 ± 0·02 ($n = 6$), FeO in glass being calculated as above. This is in good agreement with results from recent experimental studies of hydrous basaltic compositions (0·33 ± 0·05, Sisson & Grove, 1993; 0·28 ± 0·06, Barclay & Carmichael, 2004; 0·36 ± 0·04, Di Carlo *et al.*, 2006; 0·32 ± 0·04, Pichavant & Macdonald, 2007).

Volatile concentrations in experimental glasses

FTIR analyses are available for all high-pressure charges and the data (Table 5) are plotted in Fig. 2. For the crystal-free charges 17-1, 17-2 and 22-1 (Tables 2 and 5), the results give directly the H_2O and CO_2 concentrations of experimental glasses. This is also the case for charges 17-3 (a few small cpx crystals present), 17-5 (the few ~50 μm olivine crystals present were avoided from IR optical paths) and 23-1 (<3–5 wt % homogeneously distributed oxide phase present). For these charges, averages and standard deviations of multiple analytical spots (Table 5) demonstrate a homogeneous distribution of H_2O and CO_2 in the glasses. Standard deviations are on average around 2% for H_2O and 6% for CO_2, in the same range as or lower than typical precisions quoted for FTIR measurements (5–10%, Dixon *et al.*, 1995). However, for all the other charges, it was not possible to totally avoid the presence of crystals along IR optical paths and, consequently, the interpretation of the FTIR data in terms of volatile concentrations in glasses requires caution. For charges 17-4, 22-2, 22-3, 23-2 and 23-3, the presence of various amounts of crystals (cpx and Fe–Ti oxide) results in relatively high standard deviations for H_2O, up to 0·5 wt %, and in heterogeneous CO_2 concentrations (Table 5). In these charges, the CO_2 concentration reported (Table 5) is the maximum of the range. The H_2O concentration reported for charge 23-4 can be viewed as a minimum for the glass H_2O concentration, as ~13–15 wt % crystals are present in the charge. No CO_2 has been detected in that charge, which is not plotted in Fig. 2. It should be noted also that, for charge 17-4 (and 17-5), the absorbance values for the 3530 cm^{-1} H_2O band significantly exceed 1·5 (Table 5) and so the H_2O concentrations reported should be considered as minimum values.

Upon decreasing XH_2O_{in}, melt H_2O concentrations generally decrease at the three pressures investigated (Fig. 2).

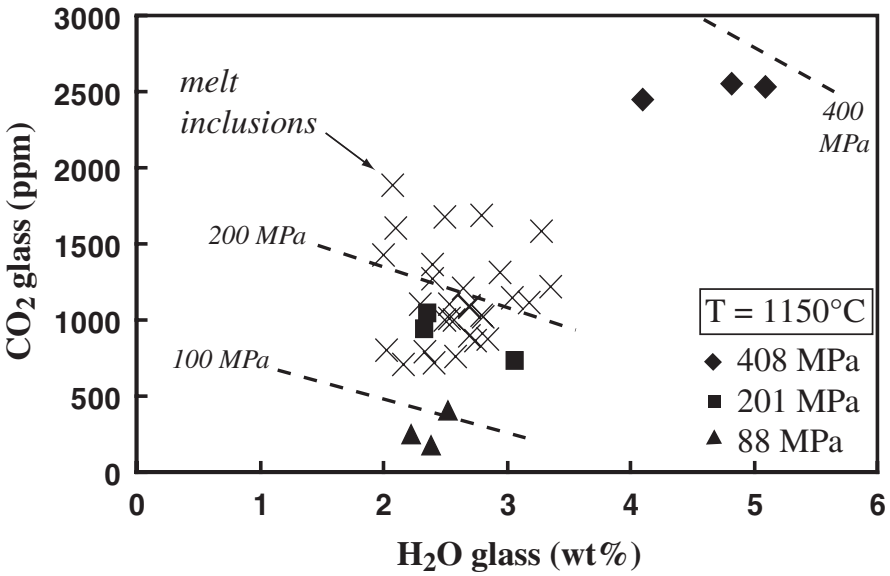

Fig. 2. H_2O and CO_2 concentrations in glasses from the fluid-present experiments and in melt inclusions from golden pumices (LP magmas). Experimental data at 1150°C and 408 MPa (diamonds), 201 MPa (squares) and 88 MPa (triangles) are from Table 5. Glass inclusion data (crosses) from Metrich *et al.* (2001, 2005) and Bertagnini *et al.* (2003). H_2O and CO_2 solubility isobars at 1150°C, and 100, 200 and 400 MPa calculated using the model of Papale *et al.* (2006) for PST-9 melt (Table 1), with FeO and Fe_2O_3 calculated for NNO + 0·5 (Kress & Carmichael, 1991).

Melt H_2O concentrations are distinctly higher at 400 MPa than at either 200 or 100 MPa. CO_2 concentrations vary little along each isobar but are markedly dependent on pressure, being in the 2500 ppm range at 400 MPa, 700–1000 ppm range at 200 MPa and 200–450 ppm range at 100 MPa (Fig. 2).

Composition of cotectic and near-cotectic melts

Compositions of selected experimental glasses are shown on a CaO vs MgO plot (Fig. 3). Experimental data points are distinguished by phase assemblage. Combining results from this study and from Di Carlo *et al.* (2006), seven fluid-absent charges at equilibrium with cpx + ol constrain the composition of cotectic liquids for a range of pressures (0·1–400 MPa), temperatures (1100–1190°C) and melt H_2O contents (0 to ~3·5 wt %). Cotectic liquids cover a substantial compositional range. On the CaO–MgO plot (Fig. 3), they follow a single, nearly linear, trend. This indicates that variations of the experimental parameters within the range above do not fundamentally change the relationships between CaO and MgO for cotectic melts. For example, the volatile-free 1190°C, 0·1 MPa and the six hydrous 1100 and 1150°C high-pressure cotectic melts (including the two 1100°C and 1150°C cotectic melts at ~400 MPa, the latter from an ol-added charge) plot on the same global trend. In detail, the three 102 and 209 MPa 1100°C cotectic points plot slightly above the main trend (Fig. 3). In the following, special attention will be given to cotectic conditions at 1150°C, as 1150°C is the temperature inferred for golden pumice magmas (Di Carlo *et al.*, 2006). The 1150°C cotectic line (Fig. 3) is defined from the three 1150°C, 408 MPa cotectic and near-cotectic charges. Given the small effect of pressure noted above, this cotectic line is considered as a reasonable approximation of cotectic conditions in the 100–400 MPa range. It should be noted that the two ol-added charges critically help to locate the cotectic, because at 1150°C and for melt H_2O contents of ~2–3·5 wt % PST-9 golden pumice melt is undersaturated with respect to olivine. The 1150°C cotectic line has a slope nearly parallel to that calculated for the cpx fractionation vector (Fig. 3). Therefore, crystallization of a significant amount of cpx is necessary before ol joins cpx on the PST-9 liquidus, as mentioned above.

The ternary ol–cpx–plag phase diagram constructed with the algorithm of Tormey *et al.* (1987) is shown in Fig. 4. Because the position of data points in this projection varies with iron redox state, the Fe^{2+}/Fe^{3+} ratios of all data points have been recalculated at NNO + 0·5 (the fO_2 inferred for golden pumice melts, Di Carlo *et al.*, 2006) for their respective experimental P and T. Again, compositions of the seven experimental glasses saturated with a cotectic ol + cpx assemblage define a single trend. The 102 and 209 MPa 1100°C cotectic points plot slightly to the right of the other points. The 1150°C cotectic line is drawn from the 1150°C, 408 MPa cotectic and near-cotectic data points. On this projection, the cpx fractionation vector is again nearly parallel to the 1150°C cotectic line drawn (Fig. 4).

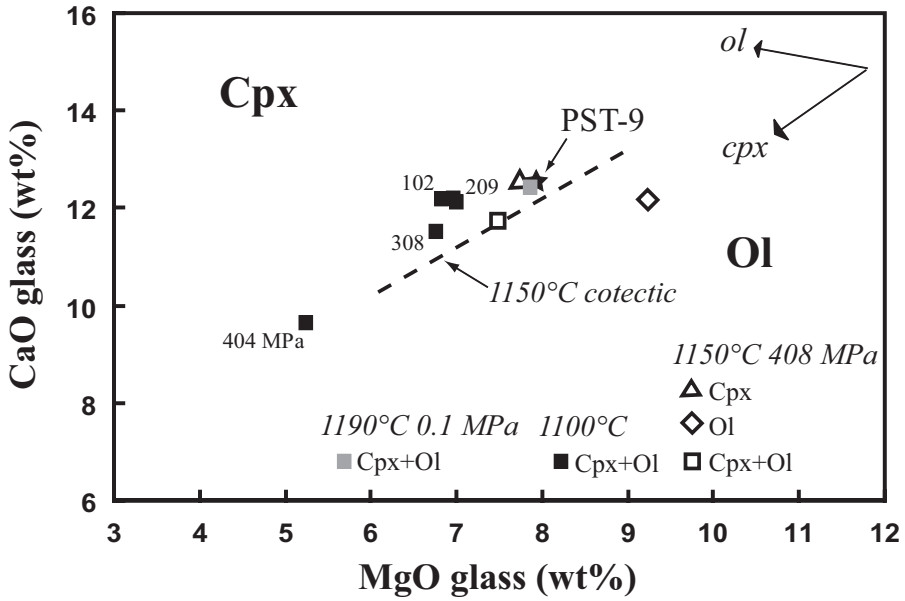

Fig. 3. CaO–MgO plot showing compositions of cotectic and near-cotectic experimental glasses. Glasses are distinguished by phase assemblage: cotectic glasses (coexisting with Cpx + Ol) are shown as squares and near-cotectic glasses (coexisting with either Cpx or Ol) as a triangle and a diamond, respectively. The black star gives the composition of PST-9 starting glass (Table 1). Experimental data at 1150, 408 MPa (open square, triangle and diamond) and 1190°C, 0·1 MPa (grey square) from Table 4. It should be noted that the two charges with ol present are the ol-seeded charges 17-4 and 17-5. Experimental data at 1100°C, and 102, 209, 308 and 404 MPa (black squares) from Di Carlo *et al.* (2006). The dashed line is the 1150°C cpx + ol cotectic drawn from the 1150°C, 408 MPa data points. Mineral crystallization vectors are calculated for Fo_{91} olivine and for the cpx in charge 17-3 (Table 4). It should be noted that the cpx crystallization vector is nearly parallel to the 1150°C cotectic.

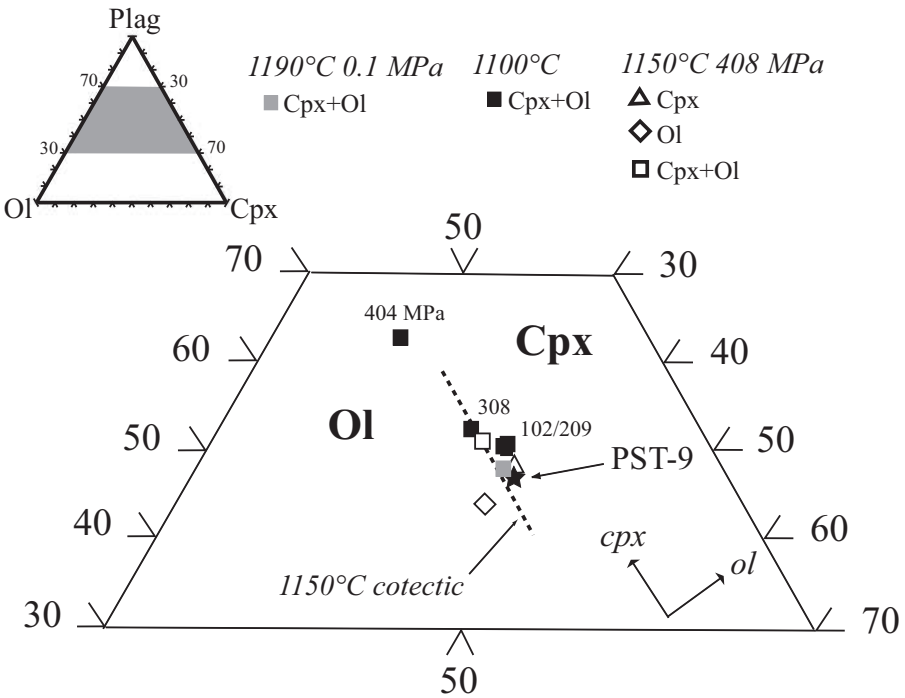

Fig. 4. Ternary ol–cpx–plg diagram constructed after Tormey *et al.* (1987) showing compositions of cotectic and near-cotectic experimental glasses. Symbols and sources of data as in Fig. 3. The cotectic is drawn from the 1150°C data points. Mineral crystallization vectors are calculated as in Fig. 3. It should be noted that the cpx crystallization vector is nearly parallel to the 1150°C cotectic.

Experimental fluid phase compositions

Compositions of fluids in the fluid-present experiments have been calculated by mass balance. Nine charges, three at each pressure (400, 200 and 100 MPa) were processed. Charge 23-4 was excluded because a significant proportion of crystals is present. The calculations were performed for three components, H_2O, CO_2 and silicate, assuming that only two phases (melt and fluid) are present in the charges (i.e. neglecting the presence of crystals). For each charge, the total masses of H_2O, CO_2 and silicate are known as well as their respective concentrations in the melt phase (Tables 4 and 5). There are four unknowns (the three H_2O, CO_2 and silicate concentrations in the fluid and the proportion of fluid phase present). A set of four equations can be written, including the three mass conservation equations and the closure equation for concentrations in the fluid phase. This set of equations was solved by minimizing the differences between starting and computed concentrations. These are <0·01 wt % for seven charges, and 0·04 and 0·07 wt % for charges 17-2 and 22-3 respectively, demonstrating the success of the mass-balance approach. Computed fluid proportions and $X H_2O$ values [equilibrium molar $H_2O/(H_2O + CO_2)$ in fluid] are given in Table 2. Compositions of experimental fluids strongly vary with pressure (Fig. 5). Decreasing pressure markedly increases $X H_2O$ and fluids evolve from dominantly CO_2-rich at 400 MPa to progressively more H_2O-rich at 200 and 100 MPa. Variations of the fluid composition are the most important above 200 MPa. Proportions of fluid phase present in the charges range from 4–6 wt % at 400 MPa (except for charge 17-2), to 7–8 wt % at 200 MPa and to 8–9 wt % at 100 MPa (Table 2). Such an evolution occurs because the solubility of H_2O in silicate melt is much higher than that of CO_2 (wt % vs ppm) at a given high pressure, and it decreases dramatically as the pressure drops to near 0·1 MPa.

DISCUSSION

Deep magma storage beneath Stromboli

The marked differences in crystallinities, volatile concentrations in glass inclusions and compositions of ol and cpx phenocrysts (including compositional gaps) between scoria and pumices (Metrich *et al.*, 2001; Bertagnini *et al.*, 2003; Francalanci *et al.*, 2004; Landi *et al.*, 2004, 2006; Cigolini *et al.*, 2008) suggest a discontinuous rather than a continuous magmatic evolution for the Stromboli feeding system. Scoria and pumices essentially record two main magmatic stages, which are thought to correspond to two local crystallization environments, each with specific physico-chemical conditions. Therefore, the Stromboli feeding system can be viewed fundamentally as a mush column (Marsh, 1996) with two rest levels. The shallow reservoir hosts crystal-rich, plagioclase-bearing, degassed magma. It sustains the present-day activity, either explosive or, more rarely, effusive (Ripepe *et al.*, 2002, 2005; Chouet *et al.*, 2003). This shallow-level reservoir is recharged by the periodic arrival of golden pumice magmas, which triggers major explosions and paroxysms (Metrich *et al.*, 2001, 2005; Bertagnini *et al.*, 2003; Francalanci *et al.*, 2004; Di Carlo *et al.*, 2006). Golden pumice magmas are sourced in a deep-seated crustal reservoir (Bertagnini *et al.*, 2003; Di Carlo *et al.*, 2006).

A precise knowledge of the physical properties of golden pumice magmas at their storage level is a prerequisite before modelling their ascent as well as their interaction and mixing with the black scoria. A set of temperatures (1140–1160°C) and pressures (100–270 MPa) has been determined previously for the near-liquidus crystallization of golden pumices in the deep reservoir, by combining experimental results, homogenization temperatures and H_2O concentrations of glass inclusions (Di Carlo *et al.*, 2006). Below, we use the fluid-present experimental data and the CO_2 concentrations in glass inclusions to more tightly estimate crystallization pressures. H_2O and CO_2 concentrations in glass inclusions from golden pumices are compared with those in glasses from the fluid-present experiments (Fig. 2). H_2O concentrations in glass inclusions and in the 88 and 201 MPa glasses overlap; the 408 MPa glasses are significantly more H_2O-rich than the inclusions. The entire range of CO_2 concentrations in glass inclusions (707–1887 ppm CO_2) is bracketed by the 88 and 408 MPa experimental data points. The glass inclusion data cluster around the 201 MPa experimental points. They plot on either side of the 200 MPa isobar (Papale *et al.*, 2006), suggesting pressures around 200 MPa for most inclusions. The few inclusions with CO_2 concentrations >1500 ppm indicate higher pressures, up to ~250 MPa. Inclusions with the lowest CO_2 concentrations plot intermediate between the 88 and 201 MPa data points and the 100 and 200 MPa isobars (Fig. 2). It should be noted that the range of pressures inferred here (150–250 MPa) lies within, but considerably tightens, the interval previously determined on the basis of the H_2O concentrations alone (100–270 MPa, Di Carlo *et al.*, 2006).

It is now becoming accepted that a fluid phase is present at depth in the reservoir source of golden pumices (e.g. Bertagnini *et al.*, 2003). For example, Scaillet & Pichavant (2005) and Burton *et al.* (2007) have suggested the presence of respectively 4 and 2·5 wt % free fluid in the Stromboli deep reservoir. Therefore, the pressures deduced above represent pressures for the equilibration of H_2O–CO_2 fluids with melts trapped as inclusions in golden pumices. These equilibration pressures can be viewed as those corresponding to the crystallization of ol in the deep reservoir, as most glass inclusions are hosted in ol. A pressure range of 150–250 MPa converts to depths of 5·7–9·4 km taking

Table 4: Experimental compositions

Charge no.	Phase	SiO_2	TiO_2	Al_2O_3	FeO	MnO	MgO	CaO	Na_2O	K_2O	Cr_2O_3	NiO	P_2O_5	Total	Mol%
Starting glass															
PST-9	gl[1](98)[2]	50·5(3)[3]	0·85(4)	15·3(3)	7·87(33)	0·16(5)	7·93(12)	12·5(2)	2·31(5)	1·87(6)	0·05(5)	0·03(3)	0·65(6)	99·4	Mg-no. 70·4
High-pressure experiments															
17-1	gl(7)	51·3(4)	0·76(2)	15·9(1)	6·49(14)	0·12(9)	8·24(8)	12·2(2)	2·38(7)	1·88(5)	0·01(2)	0·04(5)	0·64(9)	92·7	Mg-no. 76·8
17-2	gl(8)	51·2(3)	0·82(6)	15·9(2)	6·29(39)	0·14(6)	8·31(13)	12·3(2)	2·44(7)	1·85(6)	0·01(1)	0·05(4)	0·68(12)	93·7	Mg-no. 77·2
17-3	gl(10)	51·3(3)	0·86(7)	15·9(2)	6·40(34)	0·15(7)	7·74(14)	12·6(3)	2·45(7)	1·92(5)	0·01(1)	0·06(4)	0·66(8)	93·8	Mg-no. 75·4
	cpx(19)	52·5(6)	0·25(6)	2·43(52)	3·20(20)	0·11(8)	16·7(4)	22·8(5)	0·20(4)	0·03(2)	0·60(15)	0·03(5)	0·20(6)	99·1	$En_{48}Wo_{47}$
17-4	gl(8)	51·6(3)	0·92(12)	16·6(2)	6·26(9)	0·16(9)	7·48(16)	11·73(3)	2·48(10)	2·09(8)	0·03(4)	0·02(2)	n.d.	94·7	Mg-no. 74·3
	ol (3)	40·9(5)	0·01(2)	0·02(1)	9·51(86)	0·12(11)	49·4(6)	0·26(8)	0·02(2)	0·00(0)	0·06(11)	0·26(19)	n.d.	100·6	$Fo_{90·3}$
	cpx(3)	52·3(4)	0·36(7)	3·42(80)	3·93(17)	0·13(9)	16·5(4)	22·6(5)	0·24(7)	0·08(2)	0·22(18)	0·08(6)	n.d.	99·8	$En_{48}Wo_{47}$
17-5	gl(8)	51·2(4)	0·83(5)	14·9(1)	6·73(34)	0·17(12)	9·23(11)	12·2(2)	2·21(5)	1·91(6)	0·04(5)	0·07(5)	n.d.	93·2	Mg-no. 78·3
	ol (6)	41·1(4)	0·03(3)	0·04(3)	8·87(46)	0·08(5)	49·5(7)	0·14(6)	0·03(2)	0·00(0)	0·02(3)	0·30(12)	n.d.	100·2	$Fo_{90·9}$
22-1	gl(10)	50·5(3)	0·81(7)	15·4(2)	7·77(27)	0·11(9)	7·92(14)	12·7(2)	2·30(6)	1·86(12)	0·03(4)	0·03(4)	0·63(6)	95·0	Mg-no. 82·2
22-2	gl(10)	50·5(3)	0·87(6)	15·5(1)	7·87(37)	0·18(11)	7·69(11)	12·5(3)	2·37(99)	1·87(8)	0·03(4)	0·02(2)	0·62(4)	95·8	Mg-no. 80·3
	cpx(16)	48·5(6)	0·45(9)	5·37(49)	6·24(60)	0·11(8)	14·4(4)	21·8(4)	0·30(4)	0·08(3)	0·45(17)	0·03(8)	0·27(5)	98·1	$En_{45}Wo_{48}$
22-3	gl(10)	50·7(3)	0·87(8)	15·7(2)	7·64(19)	0·15(9)	7·51(9)	12·1(2)	2·47(9)	2·00(11)	0·03(4)	0·05(6)	0·67(8)	96·2	Mg-no. 80·4
	cpx(15)	48·4(6)	0·43(10)	4·95(65)	5·95(54)	0·13(8)	14·7(4)	22·3(5)	0·29(7)	0·05(6)	0·46(16)	0·06(4)	0·22(8)	98·1	$En_{45}Wo_{49}$
23-1	gl(5)	50·9(6)	0·86(9)	15·1(2)	7·68(29)	0·16(2)	7·83(21)	12·5(2)	2·41(5)	1·96(7)	0·04(5)	0·05(7)	0·55(4)	93·5	Mg-no. 83·1
23-2	gl(5)	51·5(4)	0·82(7)	15·2(1)	7·43(26)	0·12(12)	7·72(6)	12·5(2)	2·27(16)	1·81(11)	0·00(0)	0·01(2)	0·63(6)	92·3	Mg-no. 82·8
	cpx(2)	46·9(0)	0·59(27)	7·22(75)	8·34(19)	0·11(7)	14·5(3)	22·5(6)	0·39(4)	0·11(5)	0·12(9)	0·08(11)	0·37(2)	101·1	$En_{45}Wo_{50}$
23-3	gl(4)	51·0(5)	0·83(6)	15·3(1)	7·62(32)	0·12(6)	7·73(13)	12·6(2)	2·40(11)	1·84(7)	0·04(5)	0·04(4)	0·58(4)	94·2	Mg-no. 82·2
	cpx(1)	46·9	0·81	7·49	8·80	0·02	14·4	21·9	0·47	0·18	0·21	0·00	0·30	101·5	$En_{45}Wo_{49}$
23-4	gl(5)	51·2(2)	0·85(8)	16·1(2)	7·58(33)	0·15(13)	7·14(13)	11·6(2)	2·61(8)	2·1(6)	0·02(1)	0·02(4)	0·64(8)	92·5	Mg-no. 79·2
	cpx(1)	47·0	0·61	7·97	8·95	0·06	14·2	21·9	0·46	0·2	0·00	0·09	0·37	101·7	$En_{44}Wo_{49}$
0·1 MPa experiments															
1	gl(9)	51·0(5)	0·86(8)	15·5(2)	7·29(37)	0·14(10)	7·96(15)	12·4(2)	2·34(8)	1·82(7)	0·04(7)	0·05(6)	0·60(4)	98·9	Mg-no. 72·4
3	gl(9)	51·3(2)	0·83(8)	15·5(1)	7·19(37)	0·20(13)	7·78(13)	12·5(2)	2·29(9)	1·77(6)	0·03(3)	0·02(3)	0·59(5)	98·8	Mg-no. 72·4
4	gl(9)	50·9(6)	0·85(8)	15·6(2)	7·54(34)	0·14(9)	7·86(19)	12·4(2)	2·29(11)	1·75(5)	0·01(2)	0·02(3)	0·64(5)	98·9	Mg-no. 71·5
	ol(1)	41·2(0)	0·00	0·10	10·8	0·12	49·5	0·50	0·00	0·02	0·00	0·15	0·27	102·7	$Fo_{89·1}$
	cpx(1)	53·1	0·32	3·74	2·93	0·01	18·63	21·06	0·29	0·19	0·84	0	0·25	101·4	$En_{53}Wo_{43}$
5	gl(9)	51·2(4)	0·87(5)	15·8(5)	7·23(32)	0·15(9)	7·70(47)	12·1(5)	2·36(11)	1·84(12)	0·06(6)	0·05(6)	0·64(8)	98·9	Mg-no. 72·0
	ol(1)	40·4	0·02	0·10	10·8	0·21	48·5	0·51	0·01	0·01	0·05	0·14	0·36	101·0	$Fo_{88·9}$
	cpx(2)	49·7(2)	0·64(2)	6·97(28)	7·20(20)	0·12(7)	15·0(2)	19·8(3)	0·49(8)	0·29(15)	0·28(15)	0·00(0)	0·33(4)	100·9	$En_{46}Wo_{44}$
	plg(2)	49·3(7)	0·07(9)	30·0(2)	1·00(25)	0·01(1)	0·45(24)	15·2(2)	2·45(9)	0·36(7)	0·03(4)	0·02(2)	0·16(3)	99·0	$An_{75·7}Or_{2·1}$
6	gl(9)	52·7(9)	0·95(10)	16·1(4)	6·92(73)	0·20(7)	6·26(31)	10·9(5)	2·72(15)	2·50(18)	0·00(0)	0·05(9)	0·65(10)	99·5	Mg-no. 68·6
	ol(2)	41·5(4)	0·02(3)	0·10(5)	11·2(1)	0·25(3)	47·5(7)	0·55(5)	0·01(2)	0·01(1)	0·03(0)	0·13(0)	0·45(10)	101·8	$Fo_{88·3}$
	cpx(3)	49·2(1)	0·67(12)	6·70(71)	7·72(79)	0·18(8)	15·0(9)	20·1(6)	0·45(20)	0·13(18)	0·22(11)	0·00(0)	0·33(12)	100·7	$En_{46}Wo_{44}$
	plg(2)	51·0(2)	0·22(0)	28·0(6)	1·52(11)	0·01(1)	1·29(2)	14·2(4)	2·95(10)	0·76(7)	0·07(10)	0·00(0)	0·28(3)	100·3	$An_{69·5}Or_{4·5}$
8	gl(8)	52·2(43)	0·99(14)	16·0(32)	6·61(45)	0·17(8)	6·81(7)	12·0(29)	2·42(13)	2·03(14)	0·00(1)	0·06(8)	0·70(8)	99·3	Mg-no. 67·7
	ol(3)	40·5(3)	0·05(2)	0·12(4)	12·2(6)	0·21(17)	46·9(6)	0·53(4)	0·00(0)	0·02(2)	0·06(6)	0·01(2)	0·57(6)	101·1	$Fo_{87·3}$
	cpx(3)	52·8(11)	0·52(10)	4·62(90)	3·93(71)	0·04(4)	17·2(3)	20·6(7)	0·35(12)	0·11(8)	0·28(28)	0·00(0)	0·29(5)	100·7	$En_{50}Wo_{44}$
	plg(3)	50·9(4)	0·07(4)	30·4(6)	0·35(15)	0·01(2)	0·43(4)	14·7(5)	2·66(16)	0·41(2)	0·09(8)	0·01(1)	0·22(6)	100·2	$An_{73·5}Or_{2·5}$

[1]Glass analyses normalized to 100% anhydrous, with all Fe as FeO. Unnormalized total is reported. Glasses 17-4 and 17-5 normalized by assuming a P_2O_5 concentration of 0·6 wt %.
[2]Number of microprobe analyses.
[3]One standard deviation in terms of last digit.
gl, glass; cpx, clinopyroxene; ol, olivine; plg, plagioclase; n.d., not determined. Mg-number = 100 × at. Mg/(Mg + Fe) in glass with Fe = FeO. Fo = 100 × at. Mg/(Mg + Fe) in olivine, calculated with Fe = FeO_t. En = 100 × at. Mg/(Mg + Fe + Ca), Wo = 100 × at. Ca/(Mg + Fe + Ca) in pyroxene, calculated with Fe = FeO. An = 100 × at. Ca/(Ca + Na + K), Or = 100 × at. K/(Ca + Na + K) in plagioclase. FeO in glass calculated from Kress & Carmichael (1991) and FeO in cpx from the structural formula (Lindsley, 1983). PST-9 glass from Table 1 with Mg-number calculated at 1 atm, 1400°C and log fO_2 = NNO + 0·5 (Kress & Carmichael, 1991).

Table 5: FTIR data

Charge no.	n^1	Thickness (μm)	Absorbance (3530 cm^{-1})	H_2O (wt %)	Absorbance (1515 cm^{-1})	CO_2 (ppm)
17-1	2	24(1)[2]	1·151(17)[2]	5·09(5)[2]	0·133(1)[2]	2535(87)[2]
17-2	2	32(1)	1·463(29)	4·82(10)	0·180(6)	2552(192)
17-3	2	38(0)	1·469(16)	4·11(4)	0·204(6)	2452(81)
17-4	2	59(1)	1·881(240)	3·37(52)	n.d.	n.d.
17-5	3	39(1)	1·965(58)	5·35(26)	n.d.	n.d.
22-1	3	51(1)	1·478(15)	3·06(2)	0·081(5)	726(36)
22-2	5	27(1)	0·608(14)	2·33(3)	0·056[3]	933
22-3	4	27(1)	0·606(48)	2·36(22)	0·060[3]	1043
23-1	4	41(1)	0·988(18)	2·52(7)	0·037(3)	402(36)
23-2	4	51(1)	1·162(41)	2·38(14)	0·019[3]	174
23-3	3	62(2)	1·321(68)	2·23(5)	0·034[3]	250
23-4	3	27(1)	0·419(18)	1·63(0)	<0	b.d.l.

[1]Number of spectra.
[2]One standard deviation in terms of last digit.
[3]Heterogeneous CO_2 concentration (presence of crystals); the value reported is the maximum of the range.
n.d., not determined; b.d.l., below detection limit.

a density of 2·7 g/cm^3 for the crustal layer below Stromboli (Barberi *et al.*, 1994).

The viscosity and density of golden pumice magmas at their storage level have been calculated and the results are given in Table 6. Calculated viscosities and densities are 7–9 Pa s and 2·48–2·57 g/cm^3, respectively. For comparison, Cigolini *et al.* (2008) estimated a viscosity of 250 Pa s at 1150°C for golden pumice magmas with 2 wt % H_2O dissolved in the melt. It should be noted that, for the calculations in Table 6, a pressure of 200 MPa has been assumed. In fact, using averages of the H_2O and CO_2 concentrations in glass inclusions from golden pumices [2·6 wt % H_2O, 1150 ppm CO_2; data from Metrich *et al.* (2001, 2005) and Bertagnini *et al.* (2003)] yields an average fluid–melt equilibration pressure of 194 MPa with the model of Papale *et al.* (2006), the calculations being performed for a PST-9 melt at 1150°C and NNO + 0·5. Therefore, 200 MPa is a reasonable average pressure for the deep reservoir.

Fluid and gas compositions

Knowing the H_2O and CO_2 concentrations in glass inclusions, it is possible to calculate the H_2O/CO_2 ratio of fluids at equilibrium with the melts trapped as inclusions using a

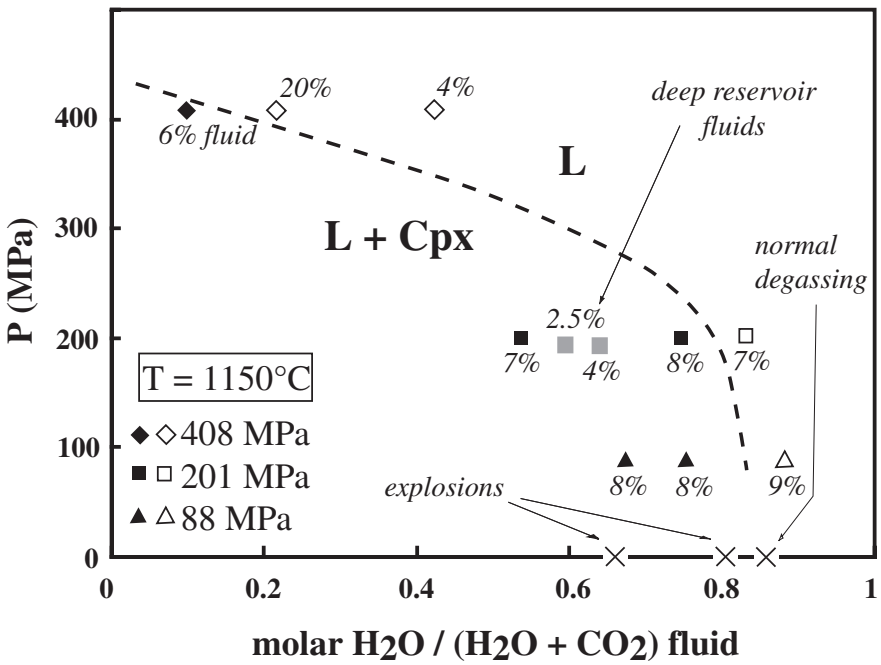

Fig. 5. Compositions [molar $H_2O/(H_2O + CO_2)$] of fluids in the 1150°C fluid-present experiments calculated by mass balance (see text). Experimental data at 408 MPa (diamonds), 201 MPa (squares) and 88 MPa (triangles) from Table 2. Open and filled experimental symbols correspond to crystal-free and crystal-bearing charges, respectively. Experimental data points are labelled with the proportion of fluid present in the charge (wt %) computed from the mass-balance calculations (Table 2). The dashed curve gives the composition of fluids coexisting with melt along the PST-9 liquidus. The compositions of deep reservoir fluids, calculated by mass balance (see text for calculation procedure), are shown as grey squares; the right square uses a fluid proportion of 4 wt % (Scaillet & Pichavant, 2005), and the left a fluid proportion of 2·5 wt % (Burton *et al.*, 2007). Natural gas compositions measured during normal degassing and explosions (Burton *et al.*, 2007) are shown (×).

Table 6: Physical properties of golden pumice (LP) magmas at their storage level

Melt	Crystals (wt %)	Fluid (wt %)	T (°C)	P (MPa)	H_2O melt (wt %)	log η[7] (Pa s)	d[8] (g/cm^3)
GP[1]	0	0	1150[5,6]	200[5,6]	2·6[5,6]	0·84	2·53
GP	5[2]	0	1150	200	2·6	0·94	2·57
GP	0	2·5[3]	1150	200	2·6	0·84	2·48
GP	5	2·5	1150	200	2·6	0·94	2·52
GP	5	4[4]	1150	200	2·6	0·94	2·48

[1]Golden pumice (Table 1).
[2]Includes 4 wt % cpx and 1 wt % ol. Density of crystals estimated to be 3·3 g/cm^3.
[3]From Burton *et al.* (2007). Density of fluid phase estimated to be 0·4 g/cm^3.
[4]From Scaillet & Pichavant (2005).
[5]from Di Carlo *et al.* (2006).
[6]This study.
[7]Melt viscosity calculated after Shaw (1972). For magma viscosity, the Einstein–Roscoe equation has been used (Scaillet *et al.*, 2000) and the presence of fluid (gas bubbles) ignored.
[8]Magma density, with melt density calculated after Ochs & Lange (1999).

solubility model such as the model of Papale *et al.* (2006). Alternatively, one can use a mass-balance approach, by considering the H_2O and CO_2 concentrations in the melt and the fluid/melt proportion at the deep reservoir level. The latter approach was adopted in this study, to maintain consistency with the determination of experimental fluid compositions. For the H_2O and CO_2 concentrations in the melt phase, we have used the average concentrations in glass inclusions (2·6 wt % H_2O and 1150 ppm CO_2, corresponding to a calculated equilibration pressure of 194 MPa; see above). For the fluid/melt proportion, values of either 4 wt % (Scaillet & Pichavant, 2005) or 2·5 wt % (Burton *et al.*, 2007) have been chosen. There are four unknowns (both the total and the fluid H_2O and CO_2 concentrations) and a set of four equations can be written (the two mass conservation equations and the two closure equations for the total and fluid concentrations). The calculated compositions ($XH_2O = 0{\cdot}59$ for 2·5 wt % fluid; 0·64 for 4 wt % fluid, Fig. 5) can be viewed as average compositions of deep reservoir fluids. They plot in the subliquidus part of the diagram, close to charge 22-3 (7 wt % fluid present). Glass in charge 22-3 has 2·4 wt % H_2O and 1043 ppm CO_2 (Table 5), nearly identical to the glass inclusion average used above; 4 wt % cpx crystals are present, consistent with the low crystallinities of golden pumices (Metrich *et al.*, 2001, 2005). This provides an independent check of the composition of deep reservoir fluids because, for an XH_2O of ~0·6 but a $P > 194$ MPa or, alternatively, a P of ~200 MPa but an $XH_2O < 0{\cdot}59$, the proportion of crystals would either decrease or increase, assuming that temperature stays constant at 1150°C. It should be noted that, for a fluid with $XH_2O = 0{\cdot}59$–$0{\cdot}64$, PST-9 golden pumice magma would become superheated above ~300 MPa (Fig. 5). Therefore, a fluid with this XH_2O must necessarily originate at pressures no greater than 300 MPa (equivalent to 11·3 km), if equilibrated with a crystal-poor golden pumice magma.

The H_2O and CO_2 concentrations of volcanic gases at Stromboli have been measured by Burton *et al.* (2007). Gases associated with quiescent degassing are relatively H_2O-rich and CO_2-poor whereas those emitted during explosions are more CO_2-rich. Gases associated with paroxysms have not yet been analyzed. The evolution of gas composition with eruptive style has been interpreted in terms of different depths of origin of the fluid (Burton *et al.*, 2007), with quiescent degassing powered by shallow and cold fluids and explosions driven by a hotter fluid phase of deeper provenance in the plumbing system. Our experimental data are in general agreement with this model (Fig. 5). Remarkably, gases emitted during normal degassing extend the composition of experimental liquidus fluids below 100 MPa. This suggests that fluid–melt equilibration at low pressures is an important factor controlling the H_2O/CO_2 ratio of these gases. The XH_2O of gases associated with the most energetic explosions approaches the XH_2O of deep reservoir fluids, although it does not quite reach it (0·66 vs 0·59–0·64, Fig. 5). These explosion gases could represent either fluids equilibrated with golden pumice magmas at pressures slightly less than 200 MPa (but no less than ~150 MPa, Fig. 2), or mixtures in various proportions between deep reservoir and shallower, more hydrous, fluids. However, the important point is that the XH_2O of the explosion gases requires that fluids similar to those equilibrated with golden pumice melts at the deep reservoir level are involved. It is concluded, therefore, that the deep reservoir fuels the normal explosive activity of Stromboli by contributing gaseous components to the shallow plumbing system. Another important inference is that volcanic gases with $XH_2O \ll \sim 0{\cdot}6$, if sampled, would necessarily signal the recharge of the deep reservoir with lower crustal or upper mantle fluids. Therefore, $H_2O/(H_2O + CO_2) = 0{\cdot}6$ appears to be a critical compositional threshold for volcanic gases at Stromboli.

Olivine stability and compositions

The new experimental results presented in this paper confirm previous conclusions about the crystallization order of PST-9 golden pumice (Di Carlo *et al.*, 2006). Clinopyroxene is the liquidus phase and olivine appears next in the crystallization sequence for all high-pressure conditions investigated, either fluid-absent and H_2O-bearing or fluid-present and H_2O- and CO_2-bearing.

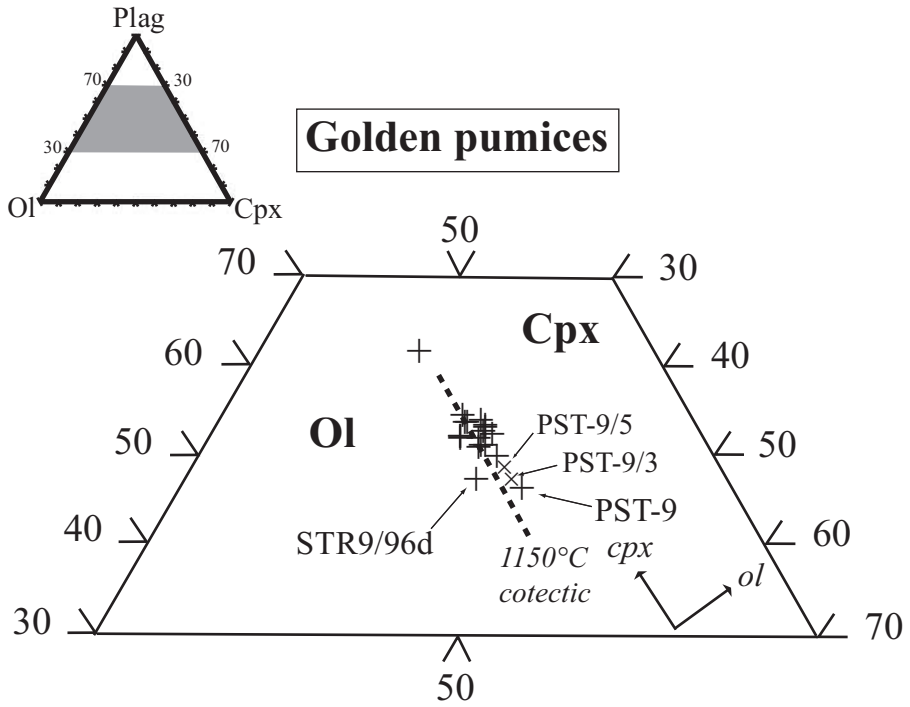

Fig. 6. Ternary ol–cpx–plg diagram constructed after Tormey *et al.* (1987) showing compositions of golden pumices (LP magmas). Data from Metrich *et al.* (2001, 2005), Bertagnini *et al.* (2003), Francalanci *et al.* (2004), Di Carlo *et al.* (2006) and M. Pompilio (personal communication). +, Golden pumices are shown as black crosses; ×, compositions obtained by subtracting either 3 or 5 wt % cpx (as in charge 17-3) from the PST-9 whole-rock analysis (respectively PST-9/3 and PST-9/5). The dashed line is the 1150°C cotectic defined in Fig. 4. Mineral crystallization vectors are calculated as in Fig. 3.

Relative to the 1150°C high-pressure cotectic, PST-9 golden pumice plots in the cpx primary field both in the CaO–MgO and ol–cpx–plag representations (Figs. 3, 4 and 6). Therefore, the conclusion about the order of crystallization of PST-9 golden pumice, previously drawn on the basis of fluid-absent experiments (Di Carlo *et al.*, 2006), is robust and independent of the high-pressure experimental conditions. This strengthens the previously noted similarity between PST-9 golden pumice and ultra-calcic magmas (or ankaramitic, used here to designate a primitive basaltic composition with cpx as the liquidus phase instead of ol at low pressures) from arc settings (Schiano *et al.*, 2000; Médard *et al.*, 2004).

The fact that clinopyroxene and olivine appear together on the 0·1 MPa PST-9 liquidus is in contrast to the high-pressure results. Although the 0·1 MPa experiments do not directly simulate the evolution of golden pumice melts, which are volatile-bearing, the 0·1 MPa phase relations need to be integrated with the high-pressure data. First, the drastic reduction of the crystallization interval upon decreasing pressure (cpx, ol and plag all appear within 10°C at 0·1 MPa) necessarily implies crystallization of cpx and ol closer to each other at 0·1 MPa than at high pressures with H_2O and CO_2. Second, olivine stability in basaltic liquids is strongly enhanced by decreasing pressure under either dry (e.g. Presnall *et al.*, 1978; Gust & Perfit, 1987) or hydrous conditions (Pichavant *et al.*, 2002*b*). Therefore, and despite that cpx crystallization can be slightly more depressed by the addition of H_2O than is ol (e.g. Di Carlo *et al.*, 2006; Pichavant & Macdonald, 2007), the simultaneous appearance of cpx and ol on the 0·1 MPa liquidus and the fact that cpx is the sole liquidus phase at high pressures are not mutually inconsistent. To check further the experimental crystallization sequence, MELTS calculations (Ghiorso & Sack, 1995) were performed for PST-9 composition (Table 4), at 0·1 MPa and NNO + 0·5. For the appearance of ol and plag, temperatures of 1190°C and 1179°C were obtained, in excellent agreement with the experimental brackets (1195–1190 and 1190–1180°C, Table 3). Thus, MELTS confirms the narrow crystallization interval obtained in the 0·1 MPa experiments. Cpx was found to crystallize as the sole liquidus phase at 1195°C, whereas in the experiments cpx is absent at this temperature, being present only at and below 1190°C (Table 3). Therefore, the MELTS calculations further support an ankaramitic signature for PST-9 golden pumice.

Olivine in golden pumices has Fo contents up to 91 (Metrich *et al.*, 2001, 2005; Bertagnini *et al.*, 2003; Francalanci *et al.*, 2004). Crystals with Fo between 83 and 87 appear in textural equilibrium with whole-rock pumices

and matrix glasses. Experimental crystallization of PST-9 at high pressures (Di Carlo *et al.*, 2006) has produced olivine in this range of compositions, with Fo up to $Fo_{87·3}$. Therefore, $Fo_{83–87}$ olivines have been interpreted as products of crystallization of golden pumice melts, and olivines with Fo >88 as xenocrysts (Bertagnini *et al.*, 2003). However, in this study, olivine compositions as high as $Fo_{89·1}$ have been obtained. This shows that olivine more magnesian than $Fo_{87·3}$ can crystallize from PST-9 or, in other words, that golden pumice melts are not limited to crystallize ol with Fo <87–88. The most magnesian ol have been obtained at 0·1 MPa (Table 3), excluding compositions from the ol-seeded charges 17-4 and 17-5. The magnesian composition of ol in the 0·1 MPa charge 4 results from equilibration with a relatively magnesian melt (Fig. 3; Tables 3 and 4). This melt is MgO-rich because, at 0·1 MPa, ol is on the liquidus together with cpx. In contrast, in the high-pressure crystallization experiments (Di Carlo *et al.*, 2006), ol is a subliquidus phase. Melts at the point of ol saturation are less MgO-rich because cpx crystallizes first on the liquidus, depleting the melt in MgO. As a result, ol crystallized from those melts is less magnesian. Therefore, the critical mechanism allowing ol more Fo-rich than 87–88 to crystallize is stabilization of ol on the PST-9 liquidus. However, such a mechanism only extends the Fo to 89–89·5 and cannot account for the presence of ol with Fo as high as 91 in golden pumices.

Cortes *et al.* (2006) reported the occurrence of unusually high-Fo (up to 96–97) olivines in various Stromboli products, including in a block ejected during the 5 April 2003 paroxysm. They interpreted these high-Fo olivines as crystallization products from a highly oxidized magma. However, the textural characteristics of these high-Fo olivines greatly differ from the Fo_{91} olivines in golden pumices. The latter are small (<1 mm) euhedral, homogeneous or normally zoned crystals (Bertagnini *et al.*, 2003; Pichavant *et al.*, in preparation) which totally lack the symplectite-like intergrowths with Fe–Ti oxides that are characteristic of the $Fo_{96–97}$ olivines (Cortes *et al.*, 2006). Cpx inclusions in the high-Fo ol described by Cortes *et al.* (2006) have high Ti and low Cr, typical of cpx crystallized well below the liquidus (Di Carlo *et al.*, 2006). This suggests that growth of their Fo-rich ol hosts took place late in the magmatic evolution. It is concluded, therefore, that the oxidation process advocated by Cortes *et al.* (2006) cannot account for the crystallization of the Fo_{91} olivines in golden pumices. These most probably crystallized from melts more primitive than golden pumices (Bertagnini *et al.*, 2003).

Petrogenesis of golden pumice (LP) magmas

The compositions of golden pumices are projected on the ternary ol–cpx–plag phase diagram (Fig. 6). For consistency with the experimental data points, all golden pumice whole-rock compositions have been recalculated at an fO_2 of NNO + 0·5, assuming $T = 1150°C$ and $P = 2$ kbar. Golden pumices cluster near the 1150°C cpx + ol cotectic line. They are spread out along the cotectic, with approximately constant ol:cpx but variable plag contents. Most pumices straddle the 1150°C cotectic line (Fig. 6) and are therefore cotectic melts, as expected for melts multiply saturated with cpx and ol. It is worth emphasizing here that the position of the cotectic line does not depend significantly on the experimental starting composition. The 1150°C cotectic has been defined from both ol-added and non ol-added PST-9 charges, and the cpx:ol ratio of experimental cotectic liquids varies very little with either pressure, temperature or melt H_2O content (Fig. 4). Therefore, the 1150°C cotectic is applicable to all LP magmas.

The position of PST-9 and STR9/96d (Francalanci *et al.*, 2004) pumices deserves special attention. As the two most primitive pumices, they plot at the low end of the plag compositional range (Fig. 6). PST-9 plots in the cpx primary field, consistent with the experimentally determined high-pressure crystallization sequence. It should be noted that compositions obtained by substracting either 3 or 5 wt % cpx to PST-9 also plot in the cpx field (Fig. 6) because the cotectic and the cpx crystallization vector are nearly parallel to each other. Thus, the crystallization sequence found for PST-9 is not the consequence of some cpx accumulation. In contrast, STR9/96d plots in the ol primary field, and so the liquidus phase in STR9/96d would be ol. In other words, the position of STR9/96d relative to the 1150°C cotectic would lead to a crystallization sequence (ol on the liquidus) different from that for PST-9 (cpx on the liquidus). This raises the question of how representative PST-9 is of the pumices, and of whether its ankaramitic character is also specific to golden pumices in general.

The answer to this question is provided by petrographical and mineralogical observations of golden pumices (Bertagnini *et al.*, 2003; A. Bertagnini, personal communication, 2006). These have shown (1) that crystallization of diopsidic cpx precedes that of ol and (2) that the proportion of cpx phenocrysts greatly exceeds that of ol. These observations, which are self-consistent, strongly suggest that the liquidus phase in golden pumice melts is cpx (and not ol). Thus, golden pumice magmas derive from parental melts lying inside the cpx primary field, a conclusion also reached by Bertagnini *et al.* (2003). Experimental results (phase equilibria and crystallization sequence) for PST-9 are consistent with those inferred for pumice parental melts. As it is the most primitive pumice, we conclude, therefore, that PST-9 is representative of golden pumice parental melts. In contrast, the position of STR9/96d appears to be unrepresentative of golden pumices in general. It probably reflects the unusual abundance of ol crystals in this pumice, as revealed by our mass-balance calculations (see above).

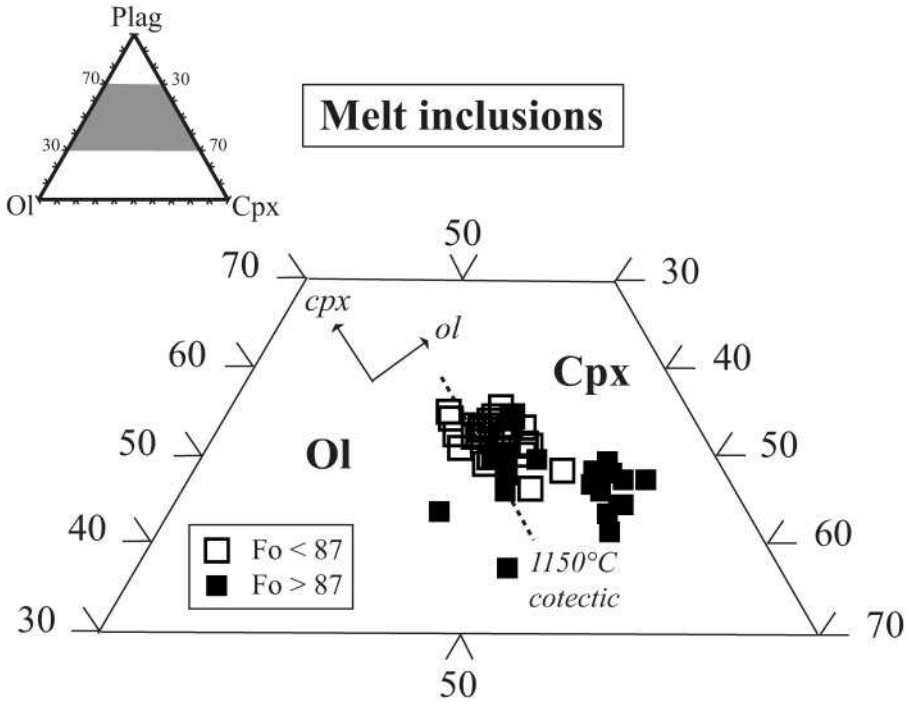

Fig. 7. Ternary ol–cpx–plg diagram constructed after Tormey *et al.* (1987) showing compositions of melt inclusions in golden pumices (LP magmas). Data from Metrich *et al.* (2001, 2005) and Bertagnini *et al.* (2003). Melt inclusions are distinguished on the basis of the forsterite content (Fo) of their host olivine. Inclusions in olivines with Fo < 87 shown as open squares and with Fo > 87 as filled squares. Two inclusions in cpx are plotted with the same symbol as the inclusions in Fo < 87 olivines. The dashed line is the 1150°C cotectic defined in Fig. 4. Mineral crystallization vectors are calculated as in Fig. 3.

Significance of the melt inclusion compositions

Compositions of glass inclusions from golden pumices are plotted in the ternary ol–cpx–plag phase diagram in Fig. 7. Glass inclusions have been subdivided into two populations, depending on their ol host Fo content (Fo < 87 and Fo > 87). Inclusions in Fo < 83 ol have been eliminated, and also inclusions showing anomalous Fe enrichments (see Bertagnini *et al.*, 2003). Only compositions recalculated for the crystallization of ol are plotted, except for two inclusions in cpx (data from Metrich *et al.*, 2001, 2005; Bertagnini *et al.*, 2003). Here also, for consistency with the other ol–cpx–plag representations (Figs. 4 and 6), melt inclusion compositions have been recalculated at an fO_2 of NNO + 0·5 (assuming $T = 1150°C$ and $P = 200$ MPa). Glass inclusion compositions show a significant spread, yet a majority plots on, or very close to, the 1150°C cotectic (Fig. 7). Therefore, most liquids trapped as inclusions in golden pumices have compositions of cotectic melts, consistent with the phenocryst assemblage of pumices. Inclusions in Fo < 87 ol plot close to the 1150°C cotectic whereas inclusions in Fo > 87 are more dispersed. In the latter population, one group plots in the cpx field away from the cotectic. These inclusions are relatively silica-poor, nepheline-normative and alkali-rich, which are typical features of ultra-calcic melts from arc settings (Schiano *et al.*, 2000; Médard *et al.*, 2004). Apart from this distinctive group, two inclusions plot in the ol primary field, away from the cotectic.

The composition of inclusions trapped in high-Fo olivines may provide clues to the origin of golden pumice magmas. Bertagnini *et al.* (2003) interpreted the group of ultra-calcic inclusions identified above as liquids parental to golden pumices, on the basis of their elevated CaO/Al_2O_3 (up to ~1) and of the high Fo contents (up to 91) of their host ol crystals. However, the composition of these trapped melts is problematic: it is clearly undersaturated with respect of olivine (Fig. 7), yet the inclusions are hosted in olivine crystals. Therefore, we suggest that these liquids correspond to boundary layer melts locally generated by cpx dissolution. Danyushevsky *et al.* (2004) have shown that anomalous glass inclusion compositions, such as ultra-calcic compositions, can originate during complex localized dissolution–reaction–mixing processes within magmatic plumbing systems. This type of process occurs at the margins of primitive magma bodies, where newly injected, hotter, magma comes into contact with previously solidified, cooler, wall-rocks, either cumulates or crystal

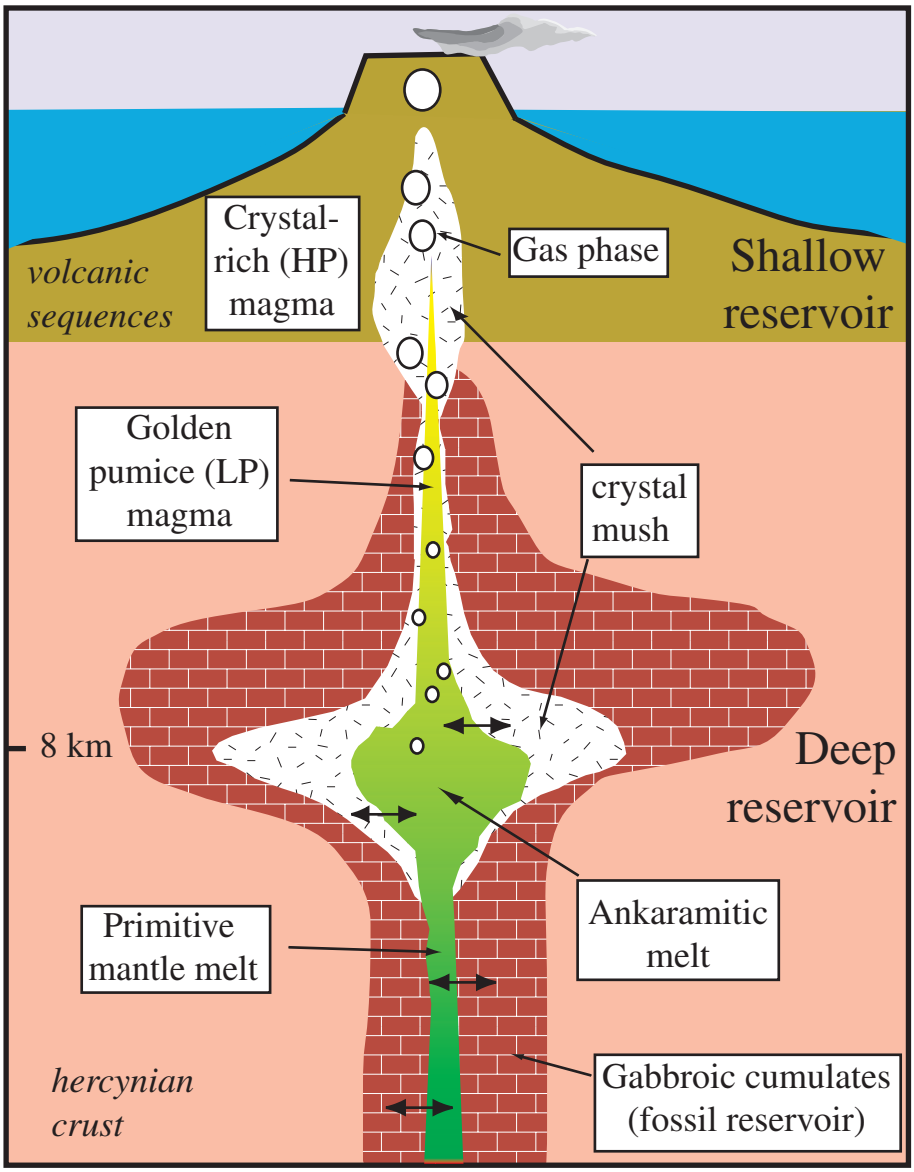

Fig. 8. Model of the internal structure of Stromboli volcano. The feeding system is a mush column (Marsh, 1996) with two local crystallization environments. The shallow reservoir hosts crystal-rich, plagioclase-bearing, degassed (HP) magma. It is recharged with the periodic arrival of golden pumice (LP) magmas, which are sourced in a deep-seated reservoir. Melt inclusions in LP magmas place the reservoir source of golden pumice magmas at a depth of ~8 km (5·7–9·4 km). A fluid phase (shown as gas bubbles) is present in the reservoir source of golden pumices. The deep reservoir contributes relatively CO_2-rich gases to the shallow plumbing system. Primitive mantle melts (shown in green) interact with cumulates and crystal mushes upon ascent (processes of wall-rock interaction and assimilation represented by double-ended arrows). Gabbroic cumulates from fossil reservoirs are shown in red and crystal mushes and cumulates from the present-day reservoir collectively in white. The ultra-calcic melts trapped as inclusions in olivine result from local melt–mush interactions in the present-day deep reservoir. Simultaneously, the primitive melts partially crystallize and mix with other melts present in the system. These different processes, combined, produce the ankaramitic melts (light green) parental to the LP magmas (yellow). Limited crystallization of these ankaramitic melts yields golden pumice (LP) magmas, which are periodically injected to higher levels. Most LP magmas have compositions of cotectic melts.

mushes (Fig. 8). Dissolution of mineral phases from the mush, mixing of reaction products with the primitive melt, and rapid crystallization of olivine from the primitive magma may lead to the entrapment of local melt compositions.

This melt–mush interaction mechanism provides an adequate explanation for the entrapment in olivine of ultra-calcic glass inclusion compositions undersaturated in olivine (Fig. 7). However, in detail, the mechanism is certainly more complex than bulk cpx dissolution alone.

Reactant phases additional to cpx are required to reproduce the trend shown by the ultra-calcic inclusions (Fig. 7). Melting or dissolution of cumulates or crystal mushes is most probably incongruent (Danyushevsky *et al.*, 2004), involving crystallization of new phases. The strong positive correlation between the S content of glass inclusions and their CaO/Al_2O_3 (Bertagnini *et al.*, 2003) suggests that S-bearing phases participate in the interaction mechanism. This would imply that the S degassed at Stromboli (e.g. Allard *et al.*, 1994) is, at least in part, recycled from older magmatic episodes.

Parental magmas

The interpretation of the ultra-calcic inclusions as local melts leaves the question of the origin of melts parental to golden pumices unresolved. On the one hand, the phase equilibria and crystallization sequence of golden pumices require ankaramitic parental melts (see also Bertagnini *et al.*, 2003). On the other hand, the occurrence of high-Fo olivines in golden pumices (up to Fo_{91}, Bertagnini *et al.*, 2003; Pichavant *et al.*, in preparation) and the presence of rare glass inclusions plotting in the ol field in the ol–cpx-plag phase diagram (Fig. 7) both imply that melts more primitive than PST-9 are present in the Stromboli feeding system. Ankaramitic compositions similar to those at Stromboli have been shown to be generated in the crust (Médard *et al.*, 2004). Primitive melts of the type precipitating the Fo_{91} crystals must have a mantle source. On this basis, it is tentatively proposed that the ankaramitic melts parental to the golden pumice magmas derive from the primitive mantle melts by a combination of crystallization, mixing, wall-rock interaction and assimilation (e.g. Francalanci *et al.*, 1989, 1993). In particular, processes of interaction between wall-rocks or cumulates from fossil reservoirs and basaltic melts may be critically important in the deep plumbing system of Stromboli (Fig. 8). For instance, the San Bartolo lavas (<5 ka) host a suite of partially reacted gabbroic inclusions that record equilibration pressures of 300–400 MPa with ascending basaltic melts (Laiolo & Cigolini, 2006; Cigolini *et al.*, 2008). Similarly, in the present-day eruptive products, the ultra-calcic melt inclusions demonstrate local interactions in the deep reservoir (150–250 MPa, Fig. 2) between crystal mushes or cumulates and basaltic melts. The LP magmas carry isotopically distinct cpx and plag interpreted as materials recycled from an old crystal mush (Francalanci *et al.*, 2005). Although the mechanism of derivation of the ankaramitic melts needs further investigation, the above lines of evidence suggest that ankaramitic signature is a relatively low-pressure (<500 MPa) overprint, and that golden pumice (LP) magmas are fundamentally hybrid products.

CONCLUSIONS

The new experimental data presented in this paper, together with previous results, allow a model for the deep feeding system of Stromboli to be refined. The feeding system can be viewed fundamentally as a two-level mush column (Marsh, 1996). The shallow reservoir, which hosts crystal-rich, plagioclase-bearing, degassed magma, sustains the present-day activity. It is recharged with the periodic arrival of golden pumice (LP) magmas, which are sourced in a mid-crustal reservoir.

(1) H_2O and CO_2 concentrations in PST-9 golden pumice glasses from near-liquidus experiments have been compared with those in melt inclusions from golden pumices. Most inclusions were trapped at pressures of 150–250 MPa. This constrains the depth of ol crystallization in the reservoir source of golden pumice magmas (5·7–9·4 km).

(2) LP magmas at their storage level have an average temperature of 1150°C, an fO_2 of NNO + 0·5, and average H_2O and CO_2 concentrations of 2·6 wt % H_2O and 1150 ppm, respectively. The deep reservoir contains a free fluid phase at 2·5–4 wt %. Viscosities and densities calculated for LP magmas are 7–9 Pa s and 2·48–2·57 g/cm^3, respectively.

(3) H_2O and CO_2 concentrations in experimental fluids equilibrated with PST-9 golden pumice melts near the liquidus were determined by mass balance. Fluids evolve from dominantly CO_2-rich at 400 MPa to progressively more H_2O-rich at 200 and 100 MPa. Calculated deep reservoir fluids have molar $H_2O/(H_2O + CO_2)$ of ~0·6. This average composition is consistent with equilibration with a near-liquidus golden pumice magma at a pressure no greater than 300 MPa. Compositions of gases emitted during explosions are relatively CO_2-rich, showing that the deep reservoir fuels the normal activity of Stromboli by contributing gaseous components to the shallow plumbing system.

(4) The new high-pressure fluid-present experiments confirm that clinopyroxene is the liquidus phase followed by olivine for PST-9 golden pumice. At 0·1 MPa, clinopyroxene and olivine crystallize together on the liquidus and olivines are more Fo-rich (up to 89·1) than at high pressures (up to 87·3, Di Carlo *et al.*, 2006). Olivines experimentally crystallized from PST-9 are never as Fo-rich than the most magnesian olivines in golden pumices (Fo_{91}).

(5) The composition of cotectic liquids cosaturated in cpx and ol has been experimentally determined. Most LP magmas plot on the cotectic and have compositions consistent with melts multiply saturated with cpx and ol. In contrast, PST-9 is representative of an earlier, less evolved magmatic stage. LP magmas derive from ankaramitic parental melts.

(6) A majority of melt inclusions in golden pumice plots on, or very close to, the cpx + ol cotectic. The ultra-calcic

compositions trapped in Fo > 87 olivines are interpreted as boundary layer melts locally generated by cpx dissolution (Danyushevsky *et al.*, 2004) rather than as melts parental to the LP magmas (Bertagnini *et al.*, 2003).

(7) The occurrence of high-Fo olivines in golden pumices and the presence of rare glass inclusions saturated in ol imply that melts more primitive than golden pumices are present in the Stromboli plumbing system. These melts evolve as a result of crystallization, mixing, wall-rock interaction and assimilation to produce the ankaramitic melts parental to the LP magmas.

ACKNOWLEDGEMENTS

The experimental study on Stromboli was partially supported by an INGV-GNV Project (Eruptive Scenarios), by Galileo funds for Italy–France scientific co-operation and by funds for international co-operation from the University of Palermo. J.-M. Bény assisted with the FTIR data collection and interpretations. Discussions with A. Bertagnini, P. Landi, P. Papale and M. Pompilio have been extremely helpful and led to substantial improvements of the paper. J. Cortes, N. Metrich, M. Rutherford and an anonymous reviewer provided constructive reviews. M. Wilson is acknowledged for her careful editorial work.

REFERENCES

Albarède F. (1995). *Introduction to Geochemical Modeling*. Cambridge: Cambridge University Press, 543 pp.

Allard, P., Carbonelle, J., Metrich, N., Loyer, H. & Zettwood, P. (1994). Sulphur output and magma degassing budget of Stromboli volcano. *Nature* **368**, 326–330.

Barberi, F., Rosi, M. & Sodi, A. (1993). Volcanic hazard assessment at Stromboli based on review of historical data. *Acta Vulcanologica* **3**, 173–187.

Barberi, F., Gandino, A., Gioncada, A., La Torre, P., Sbrana, A. & Zenucchini, C. (1994). The deep structure of the Eolian arc (Filicudi–Panarea–Vulcano sector) in light of gravity, magnetic and volcanological data. *Journal of Volcanology and Geothermal Research* **61**, 189–206.

Barclay, J. & Carmichael, I. S. E. (2004). A hornblende basalt from Western Mexico: water-saturated phase relations constrain a pressure–temperature window of eruptibility. *Journal of Petrology* **45**, 485–506.

Berndt, J., Koepke, J. & Holtz, F. (2005). An experimental investigation of the influence of water and oxygen fugacity on differentiation of MORB at 200 MPa. *Journal of Petrology* **46**, 135–167.

Bertagnini, A., Metrich, N., Landi, P. & Rosi, M. (2003). Stromboli volcano (Aeolian Archipelago, Italy): an open window on the deep-feeding system of a steady state basaltic volcano. *Journal of Geophysical Research* **108**(B7), 2336, doi:10.1029/2002JB002146.

Burnham, C.W. (1979). The importance of volatile constituents. In: Yoder, H. S., Jr (ed.) *The Evolution of Igneous Rocks*. Princeton, NJ: Princeton University Press, pp. 439–482.

Burton, M., Allard, P., Muré, F. & La Spina, A. (2007). Magmatic gas composition reveals the source depth of slug-driven Strombolian explosive activity. *Science* **317**, 227–230.

Chiarabba, C., De Gori, P. & Speranza, F. (2008). The southern Tyrrhenian subduction zone: deep geometry, magmatism and Plio-Pleistocene evolution. *Earth and Planetary Science Letters* **268**, 408–423.

Chouet, B., Dawson, P., Ohminato, T., Martini, M., Saccorotti, G., Giudicepietro, F., De Luca, G., Milana, G. & Scarpa, R. (2003). Source mechanisms of explosions at Stromboli volcano, Italy, determined from moment-tensor inversions of very-long-period data. *Journal of Geophysical Research* **108**(B1), 2019, doi:10.1029/2002JB001919.

Cigolini, C., Laiolo, M. & Bertolino, S. (2008). Probing Stromboli volcano from the mantle to paroxysmal eruptions. In: Annen, C. & Zellmer, G. F. (eds) *Dynamics of Crustal Magma Transfer, Storage and Differentiation. Geological Society, London, Special Publications* **304**, 33–70.

Cortes, J. A., Wilson, M., Condliffe, E. & Francalanci, L. (2006). The occurrence of forsterite and highly oxidizing conditions in basaltic lavas from Stromboli volcano. *Journal of Petrology* **47**, 1345–1373.

Costa, F., Scaillet, B. & Pichavant, M. (2004). Petrological and experimental constraints on the pre-eruption conditions of Holocene dacite from Volcán San Pedro (36°S, Chilean Andes) and the importance of sulphur in silicic subduction-related magmas. *Journal of Petrology* **45**, 855–881.

Danyushevsky, L. V., Leslie, R. A. J., Crawford, A. J. & Durrance, P. (2004). Melt inclusions in primitive olivine phenocrysts: the role of localized reaction processes in the origin of anomalous compositions. *Journal of Petrology* **45**, 2531–2553.

Di Carlo, I., Pichavant, M., Rotolo, S. G. & Scaillet, B. (2006). Experimental crystallization of a high-K arc basalt: the golden pumice, Stromboli volcano (Italy). *Journal of Petrology* **47**, 1317–1343.

Dixon, J. E. & Pan, V. (1995). Determination of the molar absorptivity of dissolved carbonate in basaltic glass. *American Mineralogist* **80**, 1339–1342.

Dixon, J. E., Stolper, E. M. & Holloway, J. R. (1995). An experimental study of water and carbon dioxide solubilities in mid-ocean ridge basaltic liquids. Part I: calibration and solubility models. *Journal of Petrology* **36**, 1607–1631.

Ferry, J. M. & Baumgartner, L. (1987). Thermodynamic models of molecular fluids at the elevated pressures and temperatures of the crustal metamorphism. In: Eugster, H. P. & Carmichael, I. S. E. (eds) *Thermodynamic Modeling of Geological Materials: Minerals, Fluids and Melts. Mineralogical Society of America, Reviews in Mineralogy* **17**, 323–365.

Francalanci, L., Manetti, P. & Peccerillo, A. (1989). Volcanological and magmatological evolution of Stromboli volcano (Aeolian Islands): the roles of fractional crystallization, magma mixing, crustal contamination and source heterogeneity. *Bulletin of Volcanology* **51**, 355–378.

Francalanci, L., Manetti, P., Peccerillo, A. & Keller, J. (1993). Magmatological evolution of the Stromboli volcano (Aeolian Arc, Italy): inferences from major and trace elements and Sr isotopic composition of lavas and pyroclastic rocks. *Acta Vulcanologica* **3**, 127–151.

Francalanci, L., Tommasini, S. & Conticelli, S. (2004). The volcanic activity of Stromboli in the 1906–1998 AD period: mineralogical, geochemical and isotope data relevant to the understanding of the plumbing system. *Journal of Volcanology and Geothermal Research* **131**, 179–211.

Francalanci, L., Davies, G. R., Lustenhouwer, W., Tommasini, S., Mason, P. R. D. & Conticelli, S. (2005). Intra-grain Sr isotope evidence for crystal recycling and multiple magma reservoirs in the recent activity of Stromboli volcano, southern Italy. *Journal of Petrology* **46**, 1997–2021.

Ghiorso, M. & Sack, R. (1995). Chemical mass transfer in magmatic processes. IV. A revised and internally consistent thermodynamic model for the interpolation and extrapolation of liquid–solid

equilibria in magmatic systems at elevated temperatures and pressures. *Contributions to Mineralogy and Petrology* **119**, 197–212.

Gust, D. A. & Perfit, M. R. (1987). Phase relations of a high-Mg basalt from the Aleutian island arc: implications for primary island arc basalts and high-Al basalts. *Contributions to Mineralogy and Petrology* **97**, 7–18.

Hammer, J. E., Rutherford, M. J. & Hildreth, W. (2002). Magma storage prior to the 1912 eruption at Novarupta. *Contributions to Mineralogy and Petrology* **144**, 144–162.

Holloway, J. R. (1987). Igneous fluids. In Eugster, H. P. & Carmichael, I. S. E. (eds) *Thermodynamic Modeling of Geological Materials: Minerals, Fluids and Melts. Mineralogical Society of America, Reviews in Mineralogy* 17, 211–233.

Holtz, F., Pichavant, M., Barbey, P. & Johannes, W. (1992). Effects of H_2O on liquidus phase relations in the haplogranite system at 2 and 5 kbar. *American Mineralogist* **77**, 1223–1241.

Hornig-Kjarsgaard, I., Keller, J., Koberski, U., Stadlbauer, E., Francalanci, L. & Lenhart, R. (1993). Geology, stratigraphy and volcanological evolution of the island of Stromboli, Aeolian arc, Italy. *Acta Vulcanologica* **3**, 21–68.

Kress, V. C. & Carmichael, I. S. E. (1991). The compressibility of silicate liquids containing Fe_2O_3 and the effect of composition, temperature, oxygen fugacity and pressure on their redox states. *Contributions to Mineralogy and Petrology* **108**, 82–92.

Laiolo, M. & Cigolini, C. (2006). Mafic and ultramafic xenoliths in San Bartolo lava field: new insights on the ascent and storage of Stromboli magmas. *Bulletin of Volcanology* **68**, 653–670.

Landi, P., Metrich, N., Bertagnini, A. & Rosi, M. (2004). Dynamics of magma mixing and degassing recorded in plagioclase at Stromboli (Aeolian Archipelago, Italy). *Contributions to Mineralogy and Petrology* **147**, 213–227.

Landi, P., Francalanci, L., Pompilio, M., Rosi, M., Corsaro, R. A., Petrone, C. M., Nardini, I. & Miraglia, L. (2006). The December 2002–July 2003 effusive event at Stromboli volcano, Italy: insights into the shallow plumbing system by petrochemical studies. *Journal of Volcanology and Geothermal Research* **155**, 263–284.

Lindsley, D. H. (1983). Pyroxene thermometry. *American Mineralogist* **68**, 477–493.

Longo, A., Barbato, D., Papale, P., Saccorotti, G. & Barsanti, M. (2008). Numerical simulation of the dynamics of fluid oscillations in a gravitationally unstable, compositionally stratified fissure. In: Lane, S. J. & Gilbert, J. S. (eds) *Fluid Motions in Volcanic Conduits: A Source of Seismic and Acoustic Signals. Geological Society, London, Special Publications* **307**, 33–44.

Marsh, B. (1996). Solidification fronts and magmatic evolution. *Mineralogical Magazine* **60**, 5–40.

Martel, C., Pichavant, M., Bourdier, J.-L., Traineau, H., Holtz, F. & Scaillet, B. (1998). Magma storage conditions and control of eruption regime in silicic volcanoes: experimental evidence from Mt. Pelée. *Earth and Planetary Science Letters* **156**, 89–99.

Martel, C., Pichavant, M., Holtz, F., Scaillet, B., Bourdier, J.-L. & Traineau, H. (1999). Effects of fO_2 and H_2O on andesite phase relations between 2 and 4 kbar. *Journal of Geophysical Research* **104**, 29453–29470.

Médard, E., Schmidt, M. W. & Schiano, P. (2004). Liquidus surfaces of ultracalcic primitive melts: formation conditions and sources. *Contribution to Mineralogy and Petrology* **148**, 201–215.

Metrich, N., Bertagnini, A., Landi, P. & Rosi, M. (2001). Crystallization driven by decompression and water loss at Stromboli volcano (Aeolian Islands, Italy). *Journal of Petrology* **42**, 1471–1490.

Metrich, N., Bonnin-Mosbah, M., Menez, B. & Galoisy, L. (2002). Presence of sulfite (S^{IV}) in arc magmas: implications for volcanic sulfur emissions. *Geophysical Research Letters* **29**(11), doi:10.1029/2001GL14607.

Metrich, N., Bertagnini, A., Landi, P., Rosi, M. & Belhadj, O. (2005). Triggering mechanism at the origin of paroxysms at Stromboli (Aeolian Archipelago, Italy): the 5 April 2003 eruption. *Geophysical Research Letters* **32**, L10305, doi:10.1029/2004GL022257.

Newman, S. & Lowenstern, J. B. (2002). Volatilecalc: a silicate melt–H_2O–CO_2 solution model written in Visual Basic Excel. *Computer and Geosciences* **28**, 597–604.

Ochs, F. A. & Lange, R. A. (1999). The density of hydrous magmatic liquids. *Science* **283**, 1314–1317.

Papale, P. (1999). Modeling of the solubility of two-component H_2O–CO_2 fluid in silicate liquids. *American Mineralogist* **84**, 477–492.

Papale, P., Moretti, R. & Barbato, D. (2006). The compositional dependence of the saturation surface of $H_2O + CO_2$ fluids in silicate melts. *Chemical Geology* **229**, 78–95.

Peccerillo, A., Frezotti, M. L., De Astis, G. & Ventura, G. (2006). Modeling the magma plumbing system of Vulcano (Aeolian Islands, Italy) by integrated fluid-inclusion geobarometry, petrology and geophysics. *Geology* **34**, 17–20.

Pichavant, M. & Macdonald, R. (2007). Crystallization of primitive basaltic magmas at crustal pressures and genesis of the calc-alkaline igneous suite: experimental evidence from St Vincent, Lesser Antilles arc. *Contributions to Mineralogy and Petrology* **154**, 535–558.

Pichavant, M., Martel, C., Bourdier, J.-L. & Scaillet, B. (2002*a*). Physical conditions, structure, and dynamics of a zoned magma chamber: Mount Pelée (Martinique, Lesser Antilles Arc). *Journal of Geophysical Research* **107**(B5), 2093, doi:10.1029/2001JB000315.

Pichavant, M., Mysen, B. O. & Macdonald, R. (2002*b*). Source and H_2O content of high-MgO magmas in island arc settings: an experimental study of a primitive calc-alkaline basalt from St. Vincent, Lesser Antilles arc. *Geochimica et Cosmochimica Acta* **66**, 2193–2209.

Pownceby, M. I. & O'Neill, H. St. C. (1994). Thermodynamic data from redox reactions at high temperatures. III. Activity–composition relations in Ni–Pd alloys from EMF measurements at 850–1250 K and calibration of the NiO + Ni–Pd assemblage as a redox sensor. *Contributions to Mineralogy and Petrology* **116**, 327–339.

Presnall, D. C., Dixon, S. A., Dixon, J. R., O'Donnell, T. H., Brenner, N. L., Schrock, R. L. & Dycus, D. W. (1978). Liquidus phase relations on the join diopside–forsterite–anorthite from 1 atm to 20 kbar: their bearing on the generation and crystallization of basaltic magma. *Contributions to Mineralogy and Petrology* **66**, 203–220.

Richet, P., Whittington, A., Holtz, F., Behrens, H., Ohlhorst, S. & Wilke, M. (2000). Water and the density of silicate glasses. *Contributions to Mineralogy and Petrology* **138**, 337–347.

Ripepe, M., Harris, A. J. L. & Carniel, R. (2002). Thermal, seismic and infrasonic evidences of variable degassing rates at Stromboli volcano. *Journal of Volcanology and Geothermal Research* **118**, 285–297.

Ripepe, M., Marchetti, E., Ulivieri, G., Harris, A., Dehn, J., Burton, M., Caltabiano, T. & Salerno, G. (2005). Effusive to explosive transition during the 2003 eruption of Stromboli volcano. *Geology* **33**, 341–344.

Robie, R. A., Hemingway, B. S. & Fisher, J. R. (1979). *Thermodynamic properties of minerals and related substances at 298·15 K and 1 bar (10^5 pascals) pressure and at higher temperatures. US Geological Survey Bulletin* **1452**.

Rosi, M., Bertagnini, A. & Landi, P. (2000). Onset of the persistent activity at Stromboli volcano (Italy). *Bulletin of Volcanology* **62**, 294–300.

Rutherford, M. J., Sigurdsson, H. & Carey, S. (1985). The May 18, 1980, eruption of Mount St. Helens, 1. Melt compositions and

experimental phase equilibria. *Journal of Geophysical Research* **90**, 2929–2947.

Scaillet, B. & Evans, B. W. (1999). The 15 June 1991 eruption of Mount Pinatubo. I. Phase equilibria and pre-eruption P–T–fO$_2$–fH$_2$O conditions of the dacite magma. *Journal of Petrology* **40**, 381–411.

Scaillet, B. & Pichavant, M. (2005). A model of sulphur solubility for hydrous mafic melts: application to the determination of magmatic fluid compositions of Italian volcanoes. *Annals of Geophysics* **48**, 671–698.

Scaillet, B., Pichavant, M., Roux, J., Humbert, G. & Lefèvre, A. (1992). Improvements of the Shaw membrane technique for measurements and control of fH$_2$ at high temperatures and pressures. *American Mineralogist* **77**, 647–655.

Scaillet, B., Pichavant, M. & Roux, J. (1995). Experimental crystallization of leucogranite magmas. *Journal of Petrology* **36**, 663–705.

Scaillet, B., Whittington, A., Martel, C., Pichavant, M. & Holtz, F. (2000). Phase equilibrium constraints on the viscosity of silicic magmas. II Implications for mafic–silicic mixing processes. *Transactions of the Royal Society of Edinburgh: Earth Sciences* **91**, 61–72.

Scaillet, B., Pichavant, M. & Cioni, R. (2008). Upward migration of Vesuvius magma chamber over the past 20,000 years. *Nature* **455**, 216–220.

Schiano, P., Eiler, J. M., Hutcheon, I. D. & Stolper, E. M. (2000). Primitive CaO-rich, silica-undersaturated melts in island arcs: evidence for the involvement of clinopyroxene-rich lithologies in the petrogenesis of arc magmas. *Geochemistry, Geophysics, Geosystems* **1**, 1999GC00032.

Shaw, H. R. (1972). Viscosities of magmatic liquids: an empirical method of prediction. *American Journal of Science* **272**, 870–893.

Sisson, T. W. & Grove, T. L. (1993). Experimental investigation of the role of H$_2$O in calc-alkaline differentiation and subduction zone magmatism. *Contributions to Mineralogy and Petrology* **113**, 143–166.

Speranza, F., Pompilio, M. & Sagnotti, L. (2004). Paleomagnetism of of spatter lavas from Stromboli volcano (Aeolian Islands, Italy): implications for the age of paroxysmal eruptions. *Geophysical Research Letters* **31**, L02607, doi:10.1029/20318944.

Taylor, J. R., Wall, V. J. & Pownceby, M. I. (1992). The calibration and application of accurate redox sensors. *American Mineralogist* **77**, 284–295.

Tormey, D. R., Grove, T. L. & Bryan, W. B. (1987). Experimental petrology of normal MORB near the Kane fracture zone: 22°–25°N, mid-Atlantic ridge. *Contributions to Mineralogy and Petrology* **96**, 121–139.

Watson, E. B. (1994). Diffusion in volatile-bearing magmas. In: Carroll, M. R. & Holloway, J. R. (eds) *Volatiles in Magmas. Mineralogical Society of America, Reviews in Mineralogy* **30**, 371–411.

Zhang, Y., Walker, D. & Lesher, C. E. (1989). Diffusive crystal dissolution. *Contributions to Mineralogy and Petrology* **102**, 492–513.